J. Fluid Mech. (1994), *vol.* 260, *pp.* 211–246

Nonlinear interaction of shear flow with a free surface

By ATHANASSIOS A. DIMAS
AND GEORGE S. TRIANTAFYLLOU

The Benjamin Levich Institute and Department of Mechanical Engineering,
The City College of CUNY, New York, NY 10031, USA

(Received 25 February 1992 and in revised form 26 July 1993)

In this paper the nonlinear evolution of two-dimensional shear-flow instabilities near the ocean surface is studied. The approach is numerical, through direct simulation of the incompressible Euler equations subject to the dynamic and kinematic boundary conditions at the free surface. The problem is formulated using boundary-fitted coordinates, and for the numerical simulation a spectral spatial discretization method is used involving Fourier modes in the streamwise direction and Chebyshev polynomials along the depth. An explicit integration is performed in time using a splitting scheme. The initial state of the flow is assumed to be a known parallel shear flow with a flat free surface. A perturbation having the form of the fastest growing linear instability mode of the shear flow is then introduced, and its subsequent evolution is followed numerically. According to linear theory, a shear flow with a free surface has two linear instability modes, corresponding to different branches of the dispersion relation: Branch I, at low wavenumbers; and Branch II, at high wavenumbers for low Froude numbers, and low wavenumbers for high Froude numbers. Our simulations show that the two branches have a distinctly different nonlinear evolution.

Branch I: At low Froude numbers, Branch I instability waves develop strong oval-shaped vortices immediately below the ocean surface. The induced velocity field presents a very sharp shear near the crest of the free-surface elevation in the horizontal direction. As a result, the free-surface wave acquires steep slopes, while its amplitude remains very small, and eventually the computer code crashes suggesting that the wave will break.

Branch II: At low Froude numbers, Branch II instability waves develop weak vortices with dimensions considerably smaller than their distance from the ocean surface. The induced velocity field at the ocean surface varies smoothly in space, and the free-surface elevation takes the form of a propagating wave. At high Froude numbers, however, the growing rates of the Branch II instability waves increase, resulting in the formation of strong vortices. The free surface reaches a large amplitude, and strong vertical velocity shear develops at the free surface. The computer code eventually crashes suggesting that the wave will break. This behaviour of the ocean surface persists even in the infinite-Froude-number limit.

It is concluded that the free-surface manifestation of shear-flow instabilities acquires the form of a propagating water wave only if the induced velocity field at the ocean surface varies smoothly along the direction of propagation.

1. Introduction

The interaction of sheared flows with the ocean surface is a challenging fluid-mechanics problem, which is important for several geophysical flows. Recently, observations of the ocean surface using the Synthetic Aperture Radar have added new interest on the subject by showing that significant, and sometimes intriguing, traces are left on the ocean surface by the viscous wake of ships. There is no complete theoretical explanation of such traces owing to the great complexity of the problem.

Considerable progress has been made, however, in analysing some related idealized problems, involving the surface signature of simple vortex structures (see among others Sarpkaya 1986; Bernal & Kwon 1989; Willmarth *et al.* 1989; Dommermuth & Yue 1990; Ohring & Lugt 1991). In these studies, it is found that vortices impinging upon the free surface cause localized characteristic 'scars' and 'striations'. A different vorticity/free-surface interaction problem, which can result in the generation of propagating water waves, is the nonlinear evolution of the instability of a shear flow with a free surface: It is well known that small wavy perturbations about an inviscid shear flow with an inflexional velocity profile grow exponentially in time. The question arises then as to whether the free-surface manifestation of the perturbation can reach an equilibrium state, possibly having the form of a propagating wave, once nonlinearities have saturated its growth. Knowing whether propagating waves can be generated, and their characteristics, like for instance amplitude and propagation speed, can potentially be of assistance to the wake-imaging problem.

The simplest model for this interaction is the roll-up of a submerged vortex sheet close to the ocean surface. This problem has been investigated numerically by Tryggvason (1988) and Yu & Tryggvason (1990). Their computations consistently show that the vortices formed as a result of the roll-up of a submerged vortex sheet create a steep depression on the ocean surface, which invariably evolves into a breaking wave. One may conclude therefore that the roll-up of a vortex sheet does not generate propagating surface waves (barring possibly the case of a very deeply submerged vortex sheet, where the free-surface elevation is extremely small). Modelling of a shear flow with a vortex sheet is, however, justifiable only if the wavelength of the perturbation is much longer than the thickness of the shear in the flow. For perturbations with wavelengths comparable with the thickness of the shear, it is well known that continuous variations of the initial velocity field have quite different linear and nonlinear dynamics than vortex sheets.

The linear problem of two-dimensional shear-flow/surface interaction was investigated in Triantafyllou & Dimas (1989) who found that, for every Froude number, two distinct regimes of unstable waves exist: Branch I, which appears at small wavenumbers (long wavelengths) for all Froude numbers; and Branch II, which appears at large wavenumbers (short wavelengths) for low Froude numbers, and at small wavenumbers (long wavelengths) for high Froude numbers. The shape of the eigenfunction of the two modes reveals that the Branch I instability waves are almost identical to the ones that would develop below a rigid slip-free wall, whereas the Branch II instability waves develop substantial vertical velocity at the ocean surface. Based on this, it was conjectured in Triantafyllou & Dimas (1989) that, at least at low Froude numbers, Branch II instability waves develop a more interesting free-surface manifestation than Branch I instability waves.

In this paper, we study the nonlinear evolution of the two branches of unstable waves found in Triantafyllou & Dimas (1989). The flow is assumed to be inviscid, because the Reynolds number of shear flows in the ocean is extremely high: For a ship

wake, the Reynolds number is around 10^7–10^8; for a geophysical flow, it can be much higher. The approach we follow in this paper is a direct numerical simulation of the Euler equations subject to the dynamic and kinematic boundary conditions at the free surface. The formulation and numerical technique are contained in §§2 and 3, respectively. The tests of the numerical technique are presented in §4. The results are presented in §5 and the conclusions are summarized in §6.

2. Formulation

We consider the two-dimensional interaction of an initially parallel shear flow with the free surface (see definition sketch in figure 1). The equations of motion for an incompressible inviscid fluid are the continuity equation and the Euler equations subject to the dynamic and kinematic boundary conditions on the free surface.

In two-dimensional form, the continuity equation is

$$\nabla \cdot \boldsymbol{v}' = \frac{\partial u'}{\partial x'} + \frac{\partial w'}{\partial z'} = 0, \tag{1}$$

and the momentum equations are

$$\frac{\mathrm{d}u'}{\mathrm{d}t'} = \frac{\partial u'}{\partial t'} + u'\frac{\partial u'}{\partial x'} + w'\frac{\partial u'}{\partial z'} = -\frac{\partial P'}{\partial x'}, \tag{2}$$

$$\frac{\mathrm{d}w'}{\mathrm{d}t'} = \frac{\partial w'}{\partial t'} + u'\frac{\partial w'}{\partial x'} + w'\frac{\partial w'}{\partial z'} = -\frac{\partial P'}{\partial z'} - \frac{1}{F^2}, \tag{3}$$

where lengths are non-dimensionalized with respect to the depth b of the initial shear flow (see figure 1), and velocities with respect to the free-stream velocity U_∞; x' and z' are the horizontal and vertical coordinates, respectively, t' is the non-dimensional time, $\boldsymbol{v}' = (u', w')$ is the velocity vector, P' is the pressure, and F is the Froude number of the flow, based on the depth of the initial shear flow, $F = U_\infty/(gb)^{\frac{1}{2}}$.

The dynamic and kinematic boundary conditions on the free surface are, respectively,

$$P' = 0, \quad w' = \frac{\mathrm{d}\eta}{\mathrm{d}t'} = \frac{\partial \eta}{\partial t'} + u'\frac{\partial \eta}{\partial x'} \quad \text{at} \quad z' = \eta(x', t'), \tag{4}$$

where η is the free-surface elevation.

It is more convenient to work in terms of the dynamic pressure p', defined as the pressure P' minus the hydrostatic pressure ($p' = P' - (-z'/F^2)$). Therefore, the momentum equations become

$$\frac{\mathrm{d}\boldsymbol{v}'}{\mathrm{d}t'} = \frac{\partial \boldsymbol{v}'}{\partial t'} + \boldsymbol{v}'\nabla \cdot \boldsymbol{v}' = -\nabla p', \tag{5}$$

while the boundary conditions become

$$p' = \frac{\eta}{F^2}, \quad w' = \frac{\mathrm{d}\eta}{\mathrm{d}t'} = \frac{\partial \eta}{\partial t'} + u'\frac{\partial \eta}{\partial x'} \quad \text{at} \quad z' = \eta(x', t'). \tag{6}$$

It is assumed that the water has infinite depth; so for $z' \to -\infty$, the flow becomes uniform and the dynamic pressure tends to zero. Finally, periodicity is imposed in the x-direction.

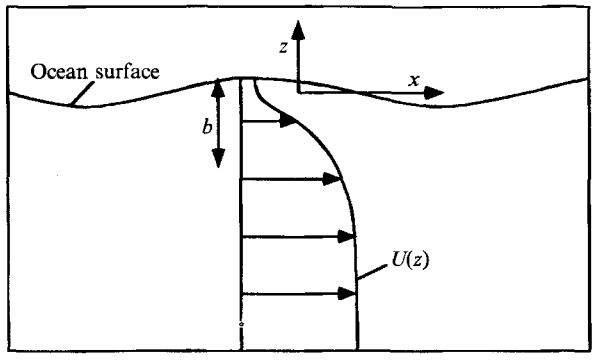

FIGURE 1. Flow domain.

In order to obtain a flow domain with boundaries fixed in time, we introduce boundary-fitted coordinates by means of the following transformation:

$$t = t', \quad x = x', \quad z = z' - \eta(x', t'). \tag{7}$$

Accordingly, the dynamic pressure and the velocity components are transformed as follows:

$$p = p', \quad u = u', \quad w = w' - \frac{\partial \eta}{\partial t'} - u' \frac{\partial \eta}{\partial x'}. \tag{8}$$

In the transformed system of coordinates, the free surface becomes the fixed plane $z = 0$. For $z < 0$, the continuity equation (1) and the momentum equation (5) are transformed as follows:

$$\nabla \cdot \boldsymbol{v} = \frac{\partial u}{\partial x} + \frac{\partial w}{\partial z} = 0, \tag{9}$$

$$\frac{\mathrm{d}\boldsymbol{v}}{\mathrm{d}t} = \frac{\partial \boldsymbol{v}}{\partial t} + \boldsymbol{v} \nabla \cdot \boldsymbol{v} = -\nabla p + \boldsymbol{A}. \tag{10}$$

The forcing term $\boldsymbol{A} = ((\partial p/\partial z)(\partial \eta/\partial x), \ -\mathrm{d}^2\eta/\mathrm{d}t^2)$ is a d'Alembert acceleration introduced by the non-inertial transformation (7).

The dynamic and kinematic boundary conditions on the free surface become

$$p = \eta/F^2, \quad w = 0 \quad \text{at} \quad z = 0, \tag{11}$$

while for $z \to -\infty$, the boundary conditions become

$$u \to U_\infty, \quad w \to -\mathrm{d}\eta/\mathrm{d}t, \quad p = \to 0 \quad \text{for} \quad z \to -\infty. \tag{12}$$

Equations (9) and (10) are solved numerically using a pseudospectral approximation method for the nonlinear terms of the momentum equation. It has been found that the pseudospectral approximation to the rotation, rather than the Reynolds stress, form of the nonlinear terms of the momentum equation does not directly cause unconditional nonlinear instability (Gotlieb & Orszag 1977).

In rotation form, the momentum equation (10) is written as

$$\frac{\partial \boldsymbol{v}}{\partial t} = \boldsymbol{v} \times \boldsymbol{\omega} - \nabla \Pi + \boldsymbol{A}, \tag{13}$$

where $\Pi = p + \frac{1}{2}(u^2 + w^2)$ is the dynamic pressure head, and $\boldsymbol{\omega}$ is the vorticity.

3. Numerical method

For the numerical solution of the equations of motion, a fractional time-step scheme is used for the temporal discretization, and a spectral approximation method for the spatial discretization (Patera 1984). The computational domain is truncated at a depth $z = -D$ in the z-direction, and has length C in the x-direction.

At the first stage of each time step, the nonlinear terms of the momentum equation (13) are treated explicitly using a third-order Adams–Bashforth scheme:

$$\frac{\hat{\boldsymbol{v}}^{n+1} - \boldsymbol{v}^n}{\Delta t} = \sum_{j=0}^{2} c_j (\boldsymbol{v} \times \boldsymbol{\omega} + \boldsymbol{A})^{n-j}, \tag{14}$$

where $c_0 = \frac{23}{12}$, $c_1 = -\frac{16}{12}$ and $c_2 = \frac{5}{12}$ are the coefficients for the third-order Adams–Bashforth scheme, and Δt is the time step. The third-order Adams–Bashforth scheme is used because of its very low dispersion errors, and the relatively large portion of the imaginary axis included within the absolute stability region of the scheme. At this stage of the time step, no boundary conditions are applied.

At the second stage of the time step, the pressure terms of the momentum equation (13) are treated implicitly:

$$\frac{\boldsymbol{v}^{n+1} - \hat{\boldsymbol{v}}^{n+1}}{\Delta t} = -\nabla \Pi^{n+1}. \tag{15}$$

The two components of (15) can be combined in the following form:

$$(\Delta \Pi)^{n+1} = \left(\frac{\partial^2 \Pi}{\partial x^2} + \frac{\partial^2 \Pi}{\partial z^2} \right)^{n+1} = \frac{1}{\Delta t} (\nabla \cdot \hat{\boldsymbol{v}} - \nabla \cdot \boldsymbol{v})^{n+1}, \tag{16}$$

which is a Poisson's equation for the pressure head. We now impose the incompressibility condition (9) on the final velocity field $\boldsymbol{v}$, and (16) becomes

$$(\Delta \Pi)^{n+1} = \frac{1}{\Delta t} (\nabla \cdot \hat{\boldsymbol{v}})^{n+1} = f^{n+1}. \tag{17}$$

Equation (17) is used to solve for the pressure head. The term in the right-hand side of this equation depends only on the intermediate velocity field $\hat{u}^{n+1}$ and $\hat{w}^{n+1}$.

The boundary conditions of the problem are applied at that stage. The dynamic and kinematic boundary conditions (11) on the free surface are combined, in terms of the pressure head, to give

$$\Pi^{n+1} = \left(\frac{\eta}{F^2} + \tfrac{1}{2} u^2 \right)^n = g^n \quad \text{at} \quad z = 0. \tag{18}$$

The momentum equation (10) is combined with the boundary condition (12), applied at the lower boundary of the computational domain, to give

$$\left(\frac{\partial \Pi}{\partial z} \right)^{n+1} = 0 \quad \text{at} \quad z = -D. \tag{19}$$

Then, the velocity field at the next time step is evaluated from (15).

The free-surface elevation is evaluated from the boundary condition (12), by solving the following first-order partial differential equation:

$$\frac{\partial \eta}{\partial t} + u(x, -D, t) \frac{\partial \eta}{\partial x} = -w(x, -D, t). \tag{20}$$

By choosing a large value for the depth D, $u(x, -D, t)$ can be replaced by U_∞. Then, (20) has constant coefficients, and its solution is simple.

For the spatial discretization, all the unknown quantities (velocity components, pressure head, vorticity) are expanded as

$$q(x, z, t) = \sum_{|l|<L} \sum_{n=0}^{N} q_{ln}(t) \exp\left(2\pi \mathrm{i} \frac{lx}{C}\right) T_n^*(z), \tag{21}$$

where L, N are the number of modes in each direction. $T_n^*(z)$ is a normalized Chebyshev polynomial of order n, defined in the $[-D, 0]$ space as

$$T_n^*(z) = T_n(s) = T_n\left(\frac{2z}{D} + 1\right), \tag{22}$$

where $-D \leqslant z \leqslant 0$ and $-1 \leqslant s \leqslant +1$.

The free-surface elevation $\eta(x, t)$ is expanded as

$$\eta(x, t) = \sum_{|l|<L} \eta_l(t) \exp\left(2\pi \mathrm{i} \frac{lx}{C}\right). \tag{23}$$

Then, at the first stage of the fractional time step, after the application of the spectral approximations, (14) becomes

$$\hat{\boldsymbol{v}}_{ln}^{n+1} = \boldsymbol{v}_{ln}^n + \Delta t \sum_{j=0}^{2} c_j (\boldsymbol{v} \times \boldsymbol{\omega} + \boldsymbol{A})_{ln}^{n-j}. \tag{24}$$

All the nonlinear terms on the right-hand side of (24) are evaluated using a pseudospectral approximation method (Orszag & Kells 1980). Thus, the rotation term, for example, is evaluated as

$$\boldsymbol{v} \times \boldsymbol{\omega} = \boldsymbol{v}(x_i, z_k, t) \times \boldsymbol{\omega}(x_i, z_k, t), \tag{25}$$

where the collocation points are

$$x_i = iC/2L \quad \text{for} \quad -L \leqslant i < L, \qquad z_k = \tfrac{1}{2}D(\cos(\pi k/N) - 1) \quad \text{for} \quad 0 \leqslant k \leqslant N. \tag{26}$$

The values of $\boldsymbol{v}(x_i, z_k, t)$ and $\boldsymbol{\omega}(x_i, z_k, t)$ in physical space are obtained from their representation in spectral space, using fast Fourier transform algorithms. Similar procedures are followed in order to evaluate the other nonlinear terms of (24), at the collocation points (26). Then, once all the nonlinear terms are represented in physical (collocation) space, again fast Fourier transform algorithms are used to obtain the nonlinear terms in the spectral (Fourier–Chebyshev) space.

At the second stage of the fractional time step, Poisson's equation (17) for the pressure head has to be solved first. In accordance with the spectral approximation (21) for the pressure head, the following expression is defined:

$$\Pi_l(z, t) = \sum_{n=0}^{N} \pi_{ln}(t)\, T_n^*(z). \tag{27}$$

Then, Poisson's equation (17), at each time step, gives a set of uncoupled equations for the coefficient-functions Π_l:

$$-\frac{4\pi^2 l^2}{C^2} \Pi_l + \frac{\mathrm{d}^2 \Pi_l}{\mathrm{d}z^2} = f_l \quad \text{for} \quad -L < l < L. \tag{28}$$

The boundary conditions (18) and (19) become

$$\Pi_l = g_l \quad \text{at} \quad z = 0, \tag{29}$$

$$\mathrm{d}\Pi_l/\mathrm{d}z = 0 \quad \text{at} \quad z = -D. \tag{30}$$

The functional expression for the solution of the above problem is

$$I_l = \int_{-D}^{0} \left(\frac{1}{2} \left(\frac{\mathrm{d}\Pi_l}{\mathrm{d}z} \right)^2 + \frac{1}{2} \frac{4\pi^2 l^2}{C^2} \Pi_l^2 + \Pi_l f_l \right) \mathrm{d}z - (\Pi_l - g_l) \frac{\mathrm{d}\Pi_l}{\mathrm{d}z} \bigg|_{z=0}. \tag{31}$$

Minimization of the functional expression (31) with respect to the coefficients of the spectral approximation (27),

$$\partial I_l / \partial \pi_{ln} = 0, \tag{32}$$

results in the following linear systems of equations for the unknown spectral coefficients π_{ln}:

$$\sum_{n=0}^{N} \pi_{ln} \left(-\frac{\pi^2 l^2 D}{C} \int_{-1}^{1} T_n T_k \, \mathrm{d}s - \frac{C}{D} \int_{-1}^{1} \frac{\mathrm{d}T_n}{\mathrm{d}s} \frac{\mathrm{d}T_k}{\mathrm{d}s} \mathrm{d}s + \frac{C}{D} n^2 + \frac{C}{D} k^2 \right)$$

$$= \frac{1}{2\Delta t} \sum_{n=0}^{N} \left(\pi \mathrm{i} l D \hat{u}_{ln} \int_{-1}^{1} T_n T_k \, \mathrm{d}s + C \hat{w}_{ln} \int_{-1}^{1} \frac{\mathrm{d}T_n}{\mathrm{d}s} T_k \, \mathrm{d}s \right) + g_l \frac{C}{D} k^2, \tag{33}$$

where $0 \leqslant k \leqslant N$. The above is an $(N+1) \times (N+1)$ system of linear equations of the form $A_l x_l = B_l$. Therefore, in order to get the pressure head in spectral space, such a linear system has to be solved for every Fourier mode. We note that the A_l matrices are time-invariant, and are inverted only once at the beginning of the computation. Subsequently, at every time step only a back substitution has to be performed (an operation of order LN^2) in order to obtain the spectral coefficients of the pressure head.

The representation of the velocity field in spectral space at the next time step is evaluated from

$$v_{ln}^{n+1} = \hat{v}_{ln}^{n+1} - \Delta t (\nabla \Pi)_{ln}^{n+1}, \tag{34}$$

where the derivatives of the pressure head in spectral space are directly evaluated from the representation of pressure head in spectral space (Orszag & Kells 1980).

The free-surface elevation, at the next time step, is evaluated from the solution of (20). Using the spectral approximation (23) of the free-surface elevation, this equation becomes

$$\frac{\mathrm{d}\eta_l}{\mathrm{d}t} + r_l \eta_l = -w(-D, t)_l = -w_l^D, \tag{35}$$

where $r_l = 2\pi \mathrm{i} U_\infty l / C$. For the solution of (35), a third-order Adams–Moulton scheme is used.

The global time accuracy of the numerical scheme is $O(\Delta t)$, even though the local error at each stage of the time step is of higher order, because the operations involved in the two stages do not commute.

There is a fundamental difficulty in computing, over long periods of time, highly nonlinear inviscid flows using spectral or pseudospectral methods: the nonlinear terms produce an energy cascade from low wavenumbers to high wavenumbers. Because a finite number of modes is retained, the cascade process accumulates energy in the highest-order modes (Myers, Taylor & Murdock 1981). Thus, the high-order modes

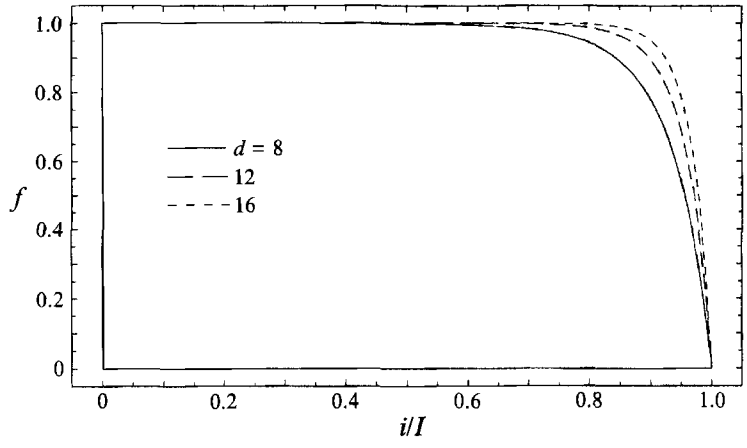

FIGURE 2. Filter function for various values of d.

grow, and the solution eventually breaks down. It is, therefore, necessary to correct the results of the calculation by filtering the energy, which is accumulated in the high-order modes. In this study, after every time step is completed, all the spectral coefficients of the u and w components of the velocity field are multiplied by a factor $f_l f_n$, and those of the free-surface elevation η by a factor f_l, where

$$f_i = \frac{1-\exp(-d(1-(i/I)^2))}{1-\exp(-d)}, \tag{36}$$

with $I = L$ for the Fourier modes, and $I = N$ for the Chebyshev modes (Haidvogel, Robinson & Schulman 1985). The value of d is adjusted so that only the highest modes are smoothed, while the large-scale features of the flow (represented by the low modes) are affected as little as possible. A plot of this filter function, for various values of d, is shown in figure 2.

For inviscid, two-dimensional flows, the vorticity ω' of the flow, prior to the application of the transformation (7), satisfies the following conservation law:

$$\frac{\mathrm{d}}{\mathrm{d}t'}\int_{V(t')} \omega'(x', t')\,\mathrm{d}V = 0, \tag{37}$$

where $V(t')$ is the flow domain.

When filtering is applied, this conservation is violated, since the filter removes an amount of vorticity from the flow, at the end of every time step. Consequently, a measure of the effect of the filter on the results of the computation is the total reduction of the value of the integral of (37), throughout the computation. In the computations reported here, the filtering parameter d is chosen such that the total reduction of (37) is not more than 1 % of its initial value.

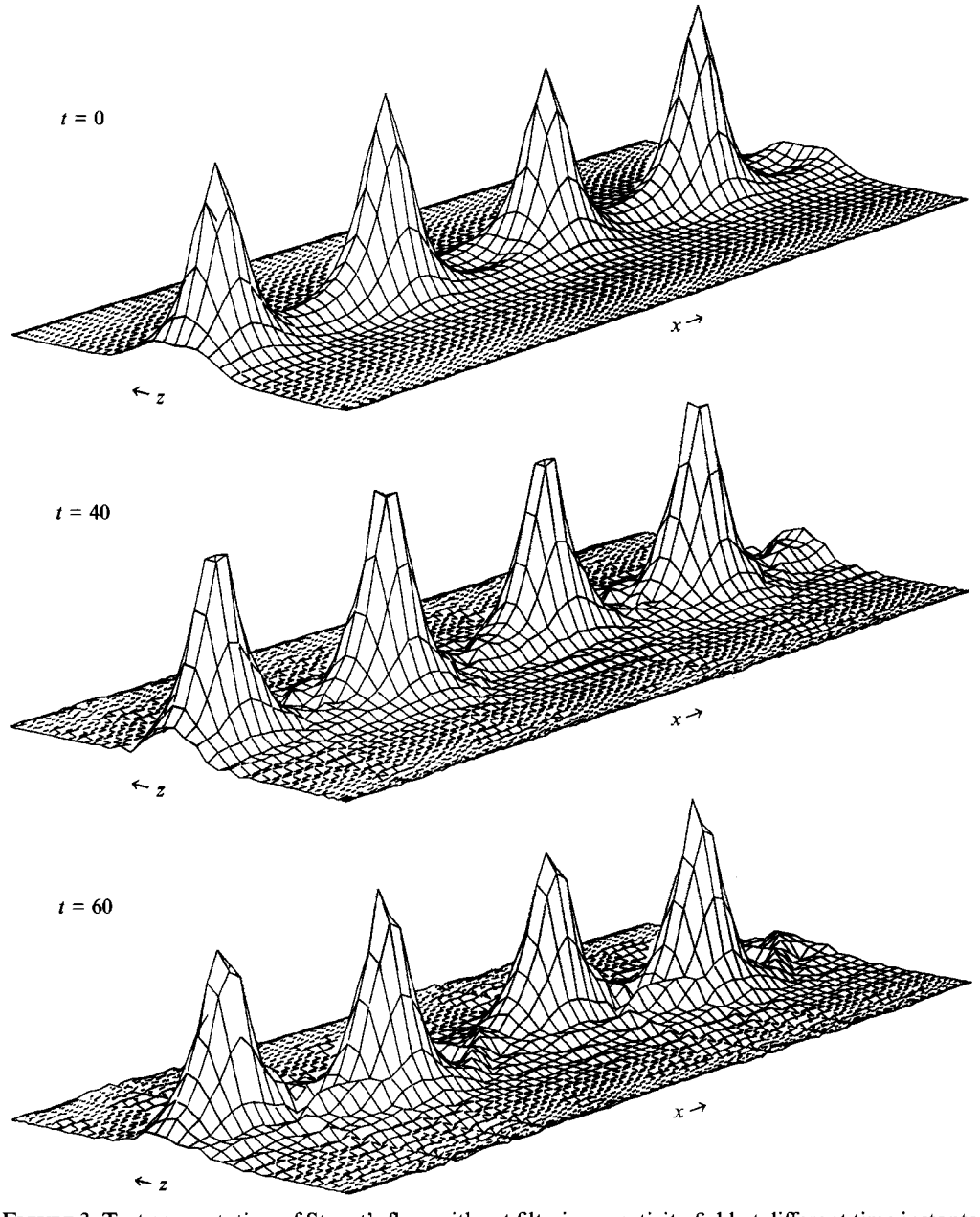

FIGURE 3. Test computation of Stuart's flow without filtering: vorticity field at different time instants. Wiggles appear at $t \approx 40$. The length in the x-direction is twice the length of the computational domain.

4. Numerical tests

Several numerical tests have been performed to test the code, a detailed presentation of which can be found in Dimas (1991). We will only present two tests here: (i) the nonlinear evolution of subharmonic instabilities of Stuart's (1967) flow, and (ii) the nonlinear evolution of a third-order Stokes wave.

Stuart's flow is a family of steady-state periodic solutions of the Euler equations (Stuart 1967). The velocity components of this flow are given by the following expressions:

$$u(x,z) = U_\infty \frac{H\sinh(kz)}{H\cosh(kz)+S\cos(kx)}, \tag{38}$$

$$w(x,z) = U_\infty \frac{S\sin(kx)}{H\cosh(kz)+S\cos(kx)}, \tag{39}$$

where H and $S=(H_2-1)^{\frac{1}{2}}$ parametrize the family of solutions, and U_∞ is the free-stream velocity ($H=1.2$ and $U_\infty=0.5$ for this study). The flow is unstable to a subharmonic disturbance flow with a wavenumber $\frac{1}{2}k$, half the wavenumber of the fundamental mode of instability (Pierrehumbert & Widnall 1982).

For the unbounded fluid flow, the hydrostatic pressure term is zero. The boundary conditions are periodicity in the x-direction, and uniform flow as $z\to\pm\infty$. For the numerical treatment, the computational domain in the z-direction is truncated at $z=-\frac{1}{2}D$ and $\frac{1}{2}D$. Therefore, the collocation points are

$$x_i = iC/2L \quad \text{for} \quad -L\leqslant i<L, \qquad z_k=\tfrac{1}{2}D\cos(\pi k/N) \quad \text{for} \quad 0\leqslant k\leqslant N. \tag{40}$$

At $t=0$, a small subharmonic disturbance flow, with velocity components $u_0(x,z)$ and $w_0(x,z)$, is superimposed on the saturated flow (38) and (39). This disturbance flow is defined by

$$u_0(x,z) = Au^*(z)\cos(\tfrac{1}{2}kx+\theta), \quad w_0(x,z) = Aw^*(z)\cos(\tfrac{1}{2}kx+\theta), \tag{41}$$

where $u^*(z)$ and $w^*(z)$ are the normalized eigenfunctions of the corresponding linear instability problem, $k=0.4446$ is the most unstable wavenumber of the mean flow (Michalke 1984), and A is a constant chosen such that the initial disturbance flow is small with respect to the saturated flow. The disturbance flow was chosen to have a phase difference $\theta=\frac{1}{2}\pi$ with the saturated flow, so that vortex pairing occurs (Metcalfe *et al.* 1987). Values of the phase difference other than integer multiples of π also lead to vortex pairing, while pairing is inhibited when $\theta=n\pi$, where n is an integer. The cases $\theta=n\pi$ are anomalous, resulting in the shredding interaction, which is rarely seen experimentally (Patnaik, Sherman & Corcos 1976).

First, we present the numerical results without filtering. The parameters for the numerical computation are: $\Delta t=0.01$, $L=16$, $N=48$, and $D=24$. The computational domain has the same length, $c=4\pi/k=28.3$, in the x-direction as the wavelength of the initial disturbance flow. Therefore, the representation of the initial velocity field in spectral space consists of non-zero coefficients for the zeroth first and second Fourier modes, and zero coefficients for all the other Fourier modes. Numerical results only up to time $t=60$ are reported, because by then the accumulation of energy at the high-order modes has started to pollute the solution. This can be seen at the plots of the vorticity field at different time instants in figure 3. The deterioration of the solution starts with the appearance of wiggles, while in spectral space, considerable noise develops in the high Fourier and Chebyshev modes.

Next, the same computation is performed up to time $t=200$, with filtering. The value of the parameter d in the filter function (36) was taken to be $d=16$. Three-dimensional plots of the vorticity field, at different time instants, are shown in figure 4. The solution in wiggle-free, and the large-scale structure of the vorticity field is unaffected. Also, the value of the integral of (37) remains almost constant (within

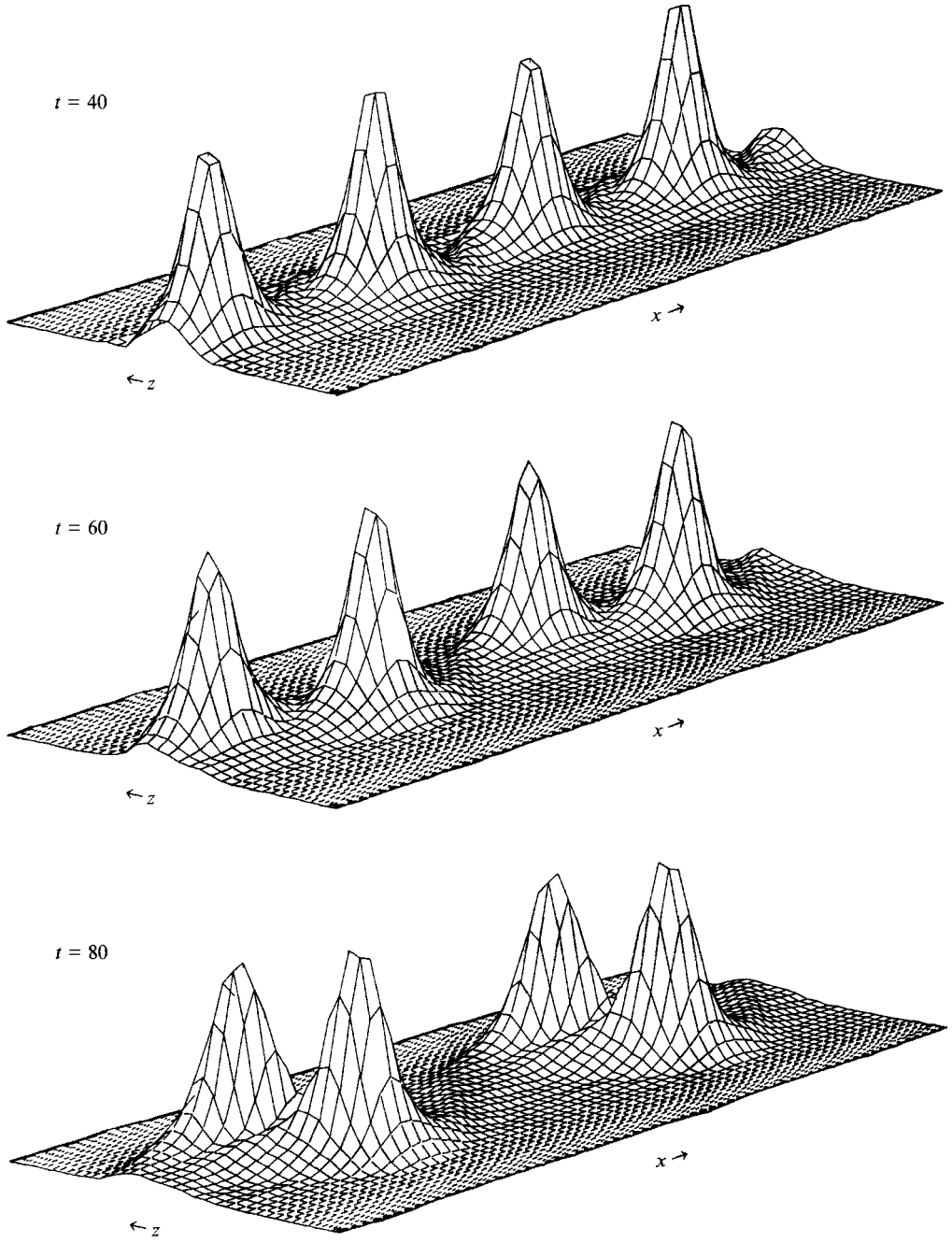

FIGURE 4. Test computation of Stuart's flow with filtering: vorticity field at different time instants. The solution remains smooth. The length in the x-direction is twice the length of the computational domain.

1/1000 of its initial value) throughout the computation. We can infer, therefore, that the filter dissipated the energy from the high-order modes without altering the large-scale features of the flow, which are represented by the low-order modes.

Vorticity contour plots of the flow, at different time instants, are shown in figure 5.

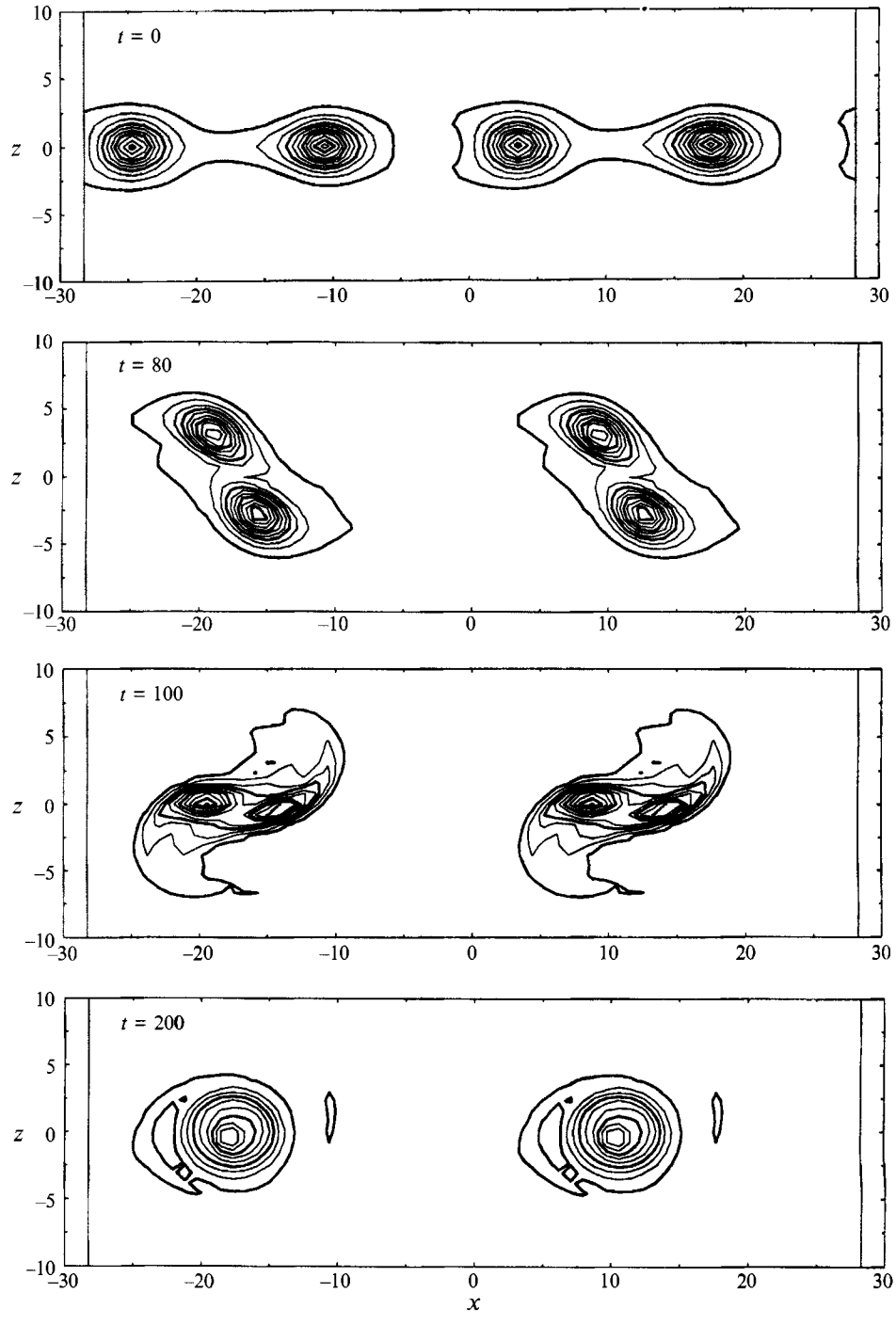

FIGURE 5. Stuart's flow, subharmonic mode: vorticity contour plots (computation with filtering) showing the vortex pairing. The length in the x-direction is twice the length of the computational domain.

Fourier modes L	Spectral coefficient $\lvert\eta_1\rvert$
8	0.099672
12	0.099909
16	0.099952
24	0.099981

TABLE 1. The magnitude of the spectral coefficient $|\eta_1|$ after eight periods T

The disturbance flow grows, and initiates the pairing of the vortices of the saturated flow. After the pairing is completed, the flow reaches another saturated quasi-steady state, which has half the wavenumber of the initial saturated state. A similar computation conducted by Metcalfe *et al.* (1987), through a direct simulation of the Navier–Stokes equations at $Re = 100$, shows large-scale features of the flow very similar to the ones in figure 5.

Next, in order to test the free-surface modelling part of our algorithm, the third-order Stokes plane progressive wave is simulated. Ideally, simulating the exact solution of the Stokes waves would be desirable, but obtaining the exact Stokes wave is a non-trivial task per se (see Dommermuth *et al.* 1988), and, instead, we used as an initial condition the third-order Stokes wave, for which analytical expressions are available.

$$u = \frac{k^{\frac{1}{2}}}{F} e^{kz} (a\cos(kx-\omega t) + a^2 k \cos^2(kx-\omega t) + a^3 k^2 (\tfrac{3}{2}\cos^2(kx-\omega t) - \tfrac{5}{8})\cos(kx-\omega t)), \tag{42}$$

$$w = \frac{k^{\frac{1}{2}}}{F} (e^{kz} - 1)(a\sin(kx-\omega t) + a^2 k \sin 2(kx-\omega t) + a^3 k^2 (\tfrac{9}{2}\cos^2(kx-\omega t) - \tfrac{5}{8})\sin(kx-\omega t)), \tag{43}$$

while the free-surface elevation is

$$\eta(x,t) = a\cos(kx-\omega t) + \tfrac{1}{2}a^2 k \cos 2(kx-\omega t) + \tfrac{3}{8}a^3 k^2 \cos 3(kx-\omega t). \tag{44}$$

For the numerical test, the parameter values Froude number $F = 1$, wavenumber $k = 1$, and wave amplitude $a = 0.2$ were selected. Several computations are performed up to time $t = 50$, which is about eight periods T of oscillations ($T = 2\pi/\omega \approx 6.16$). The truncation depth $D = 8$ is chosen so that the values of the velocity components of the flow at $z = -D$ are within 1/000 of their values at $z = -\infty$. The number of Chebyshev modes $N = 32$ is chosen so that the values of the spectral coefficients of the expansion (21) of order $n > \frac{1}{2}N$ remain at all times at most 1000 times smaller than the maximum value, which corresponds to the first mode for the u velocity component, and to the zeroth mode for the w velocity component. The filtering constant is set to $d = 16$.

In order to demonstrate the convergence properties of the numerical method, we first keep the time step $\Delta t = 0.00025$ constant, and vary the number of Fourier modes L (8, 12, 16, 24). We next keep constant the number of Fourier modes $L = 16$, and successively decrease the time step Δt (0.001, 0.0005, 0.00025).

For the first set of computations, the magnitude of the spectral coefficient of the first Fourier mode of the free-surface elevation after eight periods T is given in table 1. The plot of the corresponding relative error ϵ, with respect to the exact value $|\eta_1| = 0.1$, as

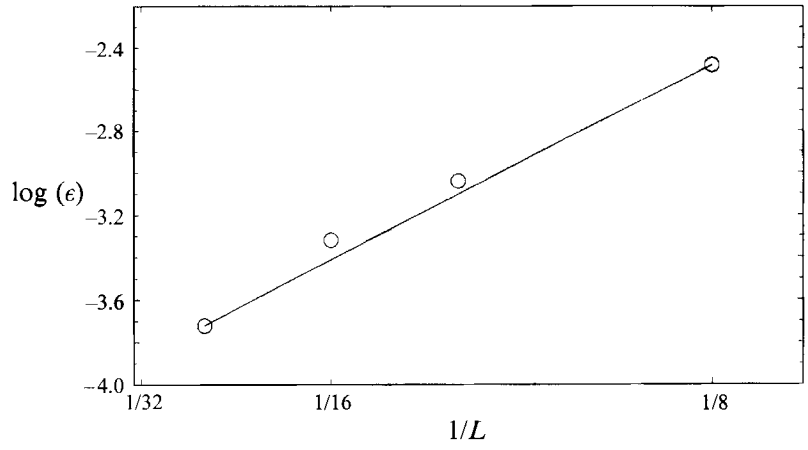

FIGURE 6. Stokes wave: relative error of the magnitude of the spectral coefficient η_1 with respect to $1/L$. The plot shows the exponential decay of the relative error.

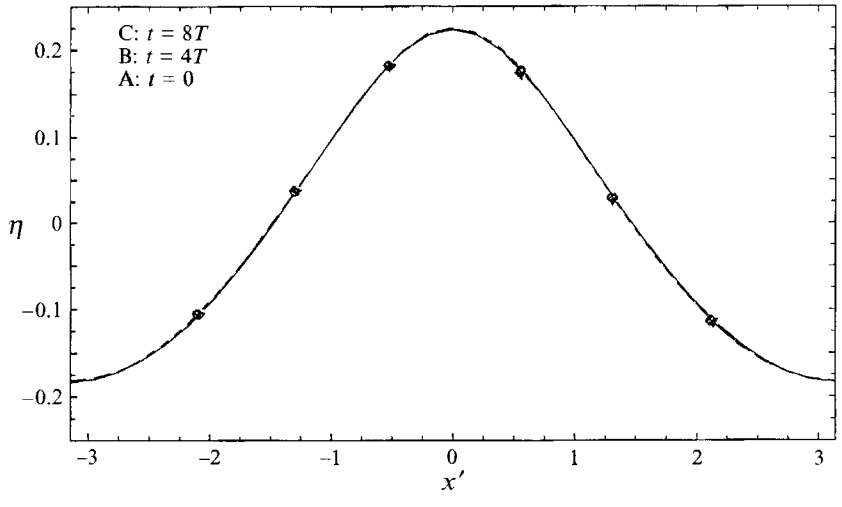

FIGURE 7. Stokes wave: free-surface elevation $\eta(x', t')$ at several time instants.

a function of $1/L$ (figure 6), shows that the numerical scheme has indeed spectral accuracy.

From the calculation with $L = 24$, the plot of the free-surface elevation η as a function of x, at several time instants, is shown in figure 7. The shape of the free-surface elevation remains practically unchanged after eight periods T of oscillations. In fact, the maximum relative error in the shape of the free-surface elevation after eight periods is 0.001.

For the second set of computations, the value of the free-surface elevation at the crest of the wave after eight periods T is given in table 2. It is shown that the convergence is indeed of $O(\Delta t)$, since by halving the time step the relative error is also approximately halved.

Time step Δt	Crest height η_{crest}	Relative error
0.001	0.22694536	
		0.00855998
0.0005	0.22501920	
		0.00444399
0.00025	0.22402364	

TABLE 2. The value of the free-surface amplitude at the crest of the wave after eight periods T.

5. Results

We now consider the interaction of a two-dimensional shear flow with a free surface. The initial velocity distribution $U(z')$ is assumed known. In this paper, the results for the following velocity profile are presented:

$$U(z') = U_\infty + (U_c - U_\infty)\frac{1}{\cosh^2(\sigma z')}, \tag{45}$$

where U_∞ is the free-stream velocity and U_c is the centreline velocity. The values $U_\infty = 1$, $U_c = 0.0012$, $\sigma = 0.88137$ are used, and the corresponding profile is shown in figure 8. This profile has been measured in the near-wake of a NACA 0003 hydrofoil in unbounded fluid by Mattingly & Criminale (1972).

5.1. *Summary of linear theory*

For the linear stability analysis of the flow, a small disturbance flow $(u'(x', z', t'), w'(x', z', t'))$ is superimposed on the initial mean flow $U(z')$. The evolution of the unsteady disturbance flow is studied by linearizing the equations of motion around the mean velocity profile. Because the mean flow is parallel, wavy perturbations can be considered in the form:

$$u'(x', z', t') = u^*(z')\exp(\mathrm{i}(kx' - \omega t')), \quad w'(x', z', t') = w^*(z')\exp(\mathrm{i}(kx' - \omega t')), \tag{46}$$

where k is the wavenumber and ω is the frequency. An eigenvalue problem for the frequency ω is then obtained, consisting of Rayleigh's equation subject to the linearized free-surface boundary conditions. The eigenvalue problem can be solved numerically by approximating with a generalized algebraic eigenvalue problem. A detailed stability analysis can be found in Triantafyllou & Dimas (1989). We summarize here only the main results.

An inflexional shear flow with a free surface has two instability modes: one at low wavenumbers, that we refer to as Branch I, and one at high wavenumbers, of order $k \approx 1/F^2$, that we refer to as Branch II. Branch I is to within an error of order F^2 the same as the antisymmetric stream function instability in infinite fluid, whereas Branch II is a 'hybrid' mode, in-between the symmetric and antisymmetric stream function modes in unbounded fluid. As the Froude number increases, the growth rates and the range of unstable wavenumbers of the Branch I instability decrease. On the other hand, the growth rates of the Branch II instability increase, and the range of the unstable wavenumbers increases and moves to the low-wavenumber region. For $F = \infty$, the Branch II instability of the free-surface flow is the same as the symmetric stream function instability of the corresponding unbounded flow, whereas Branch I disappears.

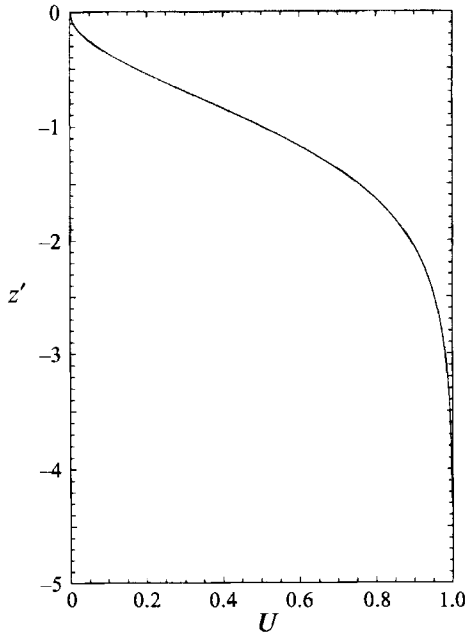

FIGURE 8. Mean velocity profile.

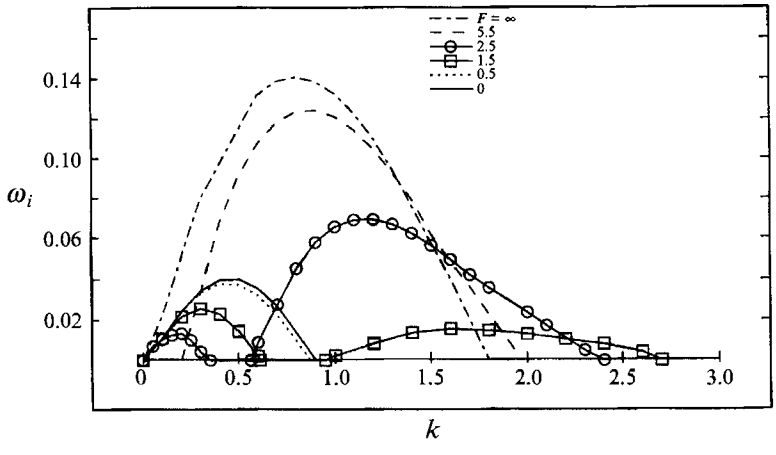

FIGURE 9. Temporal instability curves for several Froude numbers.

This behaviour is demonstrated in figure 9, where the growth rates ($\omega_i = \mathrm{Im}(\omega)$ versus $k = \mathrm{Re}(k)$) for various Froude numbers are shown for the profile (45).

5.2. *Nonlinear evolution of Branch I instability*

We start with the nonlinear evolution of the Branch I instability for the flow (velocity profile (45)). The disturbance introduced at $t' = 0$ has the form of the fastest growing wave of the linear problem. In other words, the two velocity components are given by

$$u'_0(x', z') = \mathrm{Re}\{u^*(z')\exp(\mathrm{i}kx')\}, \quad w'_0(x', z') = \mathrm{Re}\{w^*(z')\exp(\mathrm{i}kx')\}, \tag{47}$$

where k is the wavenumber of the instability, and $u^*(z')$, $w^*(z')$ are found from the

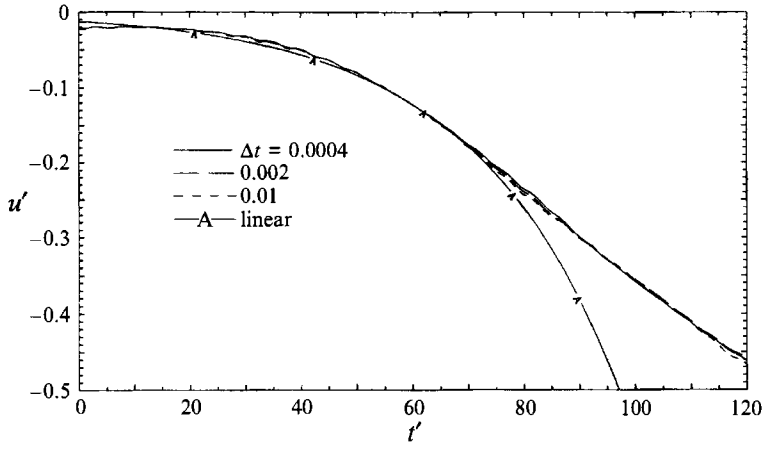

FIGURE 10. Branch I, $F = 0.5$: horizontal velocity $u'(x', z', t')$ of the perturbation flow at the collocation point (x_0, z_0). The linear-regime exponential growth saturates after time $t' \approx 60$.

solution of Rayleigh's equation subject to the linearized conditions at the free surface. The free-surface elevation associated with the disturbance is given by

$$\eta_0(x') = \mathrm{Re}\{\alpha \exp(\mathrm{i}kx')\}, \tag{48}$$

where α is the complex amplitude of the free-surface elevation. Since $u^*(z')$, $w^*(z')$ and α are obtained from the solution of a linear eigenvalue problem, they can be evaluated to within an arbitrary multiplying constant. The constant is chosen so that the magnitude of the disturbance velocity field is much smaller than the magnitude of the velocity in the parallel shear flow (except at the points where the latter vanishes). The initial disturbance flow is chosen such that the maximum velocity of the initial disturbance flow is about 1% of the free-stream velocity U_∞. The computations are performed in an inertial frame of reference moving at a speed equal to the phase velocity $c_r = \omega_r/k$ of the linear instability, and the results are presented in the same moving frame. The initial mean flow in the moving frame is $U(z') - c_r$.

The linear stability results for the most unstable wave at Froude number $F = 0.5$ are: $k = 0.4$, $\omega_r = 0.1098$ $(T = 2\pi/\omega_r = 57.2)$, $\omega_i = 0.038$. For the numerical solution, several computations are performed, where the time step Δt takes the values 0.01, 0.002, 0.0004, and the number of Fourier modes L takes the values 16, 32, while the other parameters are: $N = 48$, $D = 12$, $C = 2\pi/k = 15.7$ and $d = 16$. The truncation depth D, and the number of Chebyshev modes N are chosen so that all flow components have negligible z-dependence for $z < -\frac{1}{2}D$, and the spectral coefficients of order $n > \frac{1}{2}N$ remain small at all times.

The plot of the horizontal velocity u' of the perturbation flow (defined as the total flow minus the mean flow) at the collocation point (x_0, z_0) of the moving frame, as a function of time, is shown in figure 10. Initially, the growth of the numerical solution follows the linear theory prediction, but eventually the nonlinear terms become significant and the solution deviates from the linear theory.

The free-surface elevation as a function of x', at different instants in time, is shown in figure 11. During the early stages of the evolution, where the evolution is basically linear, the free-surface elevation has a sinusoidal shape. Subsequently, as nonlinear terms become significant, the free-surface elevation acquires a highly non-sinusoidal shape with steep slopes. In particular, a very sharp depression of the free-surface

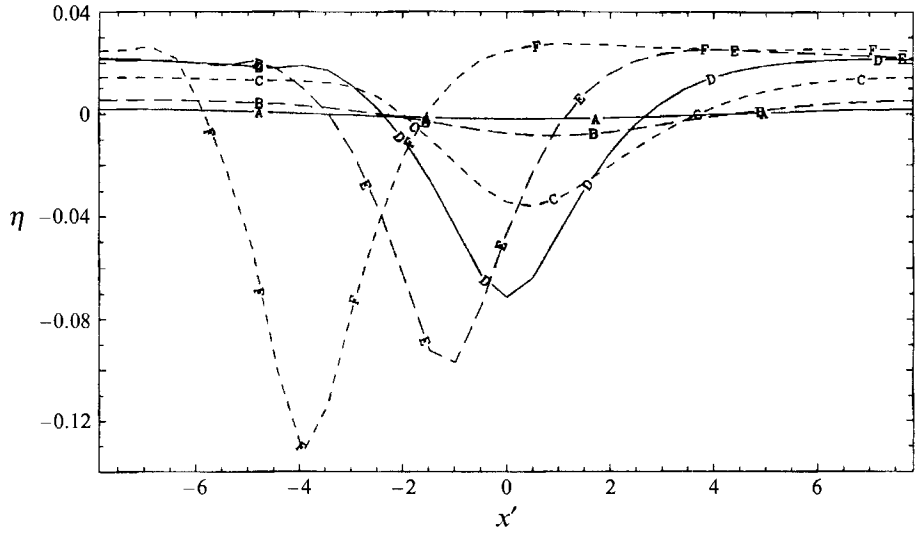

FIGURE 11. Branch I, $F = 0.5$: free-surface elevation $\eta(x', t')$ at different time instants. The wave height is very small compared to the wavelength, even just before breaking. A, $t' = 0$; B, 50; C, 100; D, 150; E, 200; F, 260.

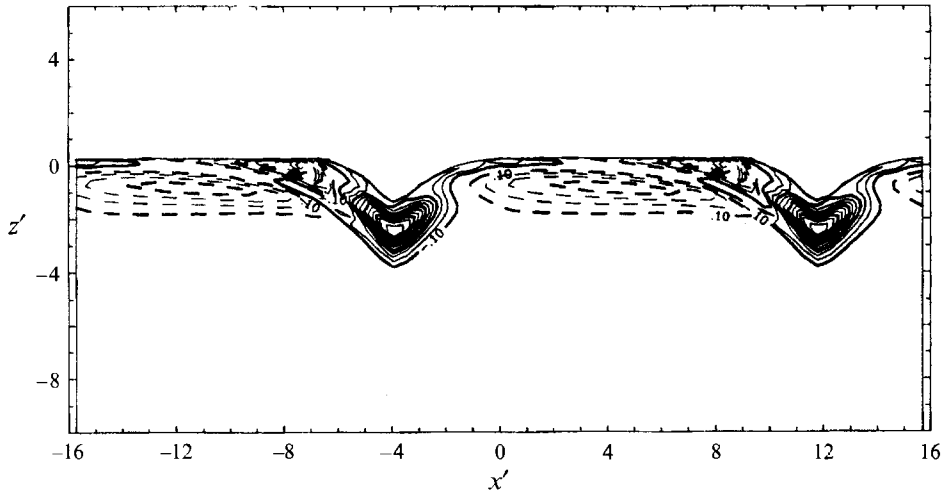

FIGURE 12. Branch I, $F = 0.5$: vorticity contour plot of the perturbation flow (the free-surface elevation is amplified by a factor of ten) at time $t' = 260$. It shows the presence of two vortices per wavelength with opposite signs. Solid lines represent counterclockwise rotation, dashed lines represent clockwise rotation, the interval between contour levels is 0.1, and the length in the x-direction is twice the length of the computational domain.

elevation develops at the trough of the wave, and it becomes so large that at time $t' \approx 260$ the computer program crashes. In the spectral space, as we approach the time of crashing, there is a simultaneous amplitude increase in all Fourier modes. This behaviour is quite different than the one encountered in the energy cascade process, described in §4, where accumulation of energy started only in the high Fourier modes, and eventually destroyed the solution. In the present case, the action of filtering cannot stop the growth of the Fourier modes, which is clearly caused by the fact that the slope of the wave approaches infinity at some point.

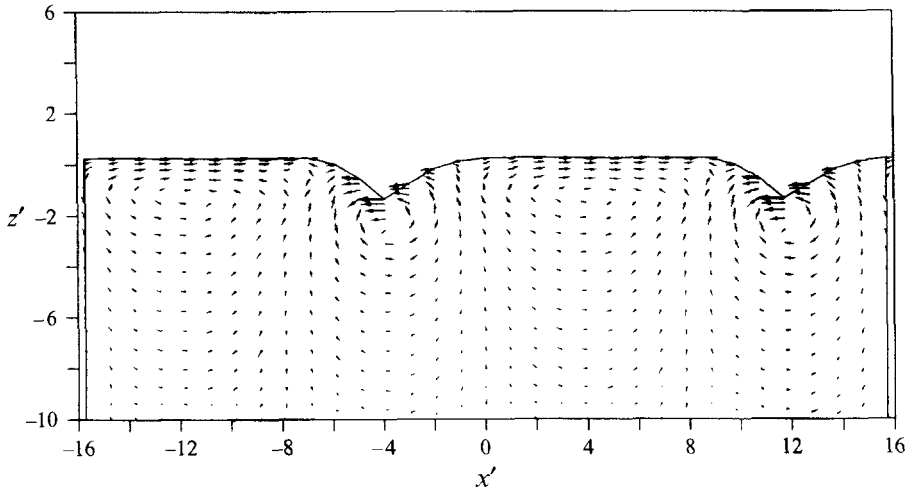

FIGURE 13. Branch I, $F = 0.5$: velocity vector plot of the perturbation flow (the free-surface elevation is amplified by a factor of ten) at time $t' = 260$. Sharp horizontal velocity shear develops at the free surface. The length in the x-direction is twice the length of the computational domain.

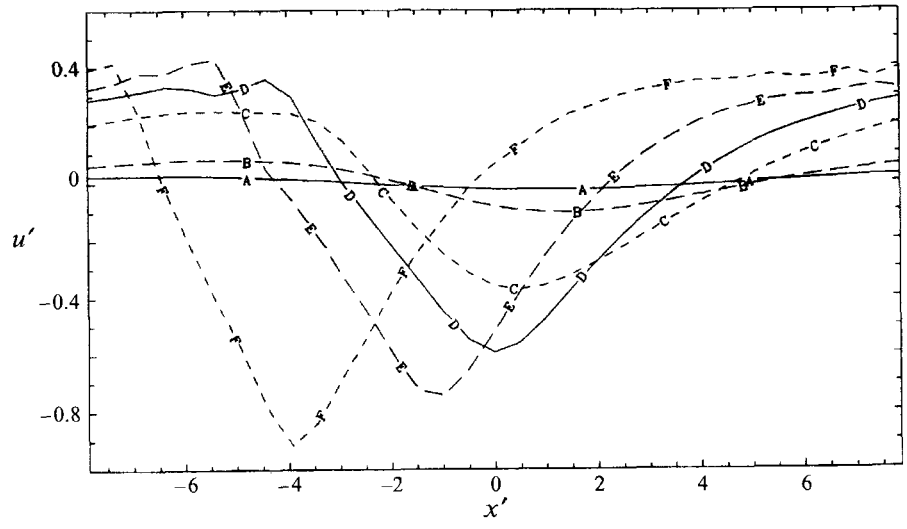

FIGURE 14. Branch I, $F = 0.5$: horizontal velocity $u'(x', z' = \eta, t')$ of the perturbation flow at the free surface and at different time instants. Sharp shear develops before the program crashes. Curves as in figure 11.

For different combinations of Δt and L, we observe the following behaviour. For the same number $L = 16$ of Fourier modes, as the time step decreases from 0.01 to 0.002 to 0.0004, the program crashes at a later time, $t' \approx 120$, $t' \approx 140$, $t' \approx 260$, respectively, but for the common time interval the results are practically the same. Similarly, for the computations with time step $\Delta t = 0.002$, as the number of Fourier modes doubles from 16 to 32, the computer crashes at a later time, $t' \approx 120$, $t' \approx 140$, respectively, but, again, for the common time interval the results are the same. The delay of the crashing is attributed to the fact that, by reducing the size of the time step or increasing the number of Fourier modes, the computation can capture steeper slopes of waves.

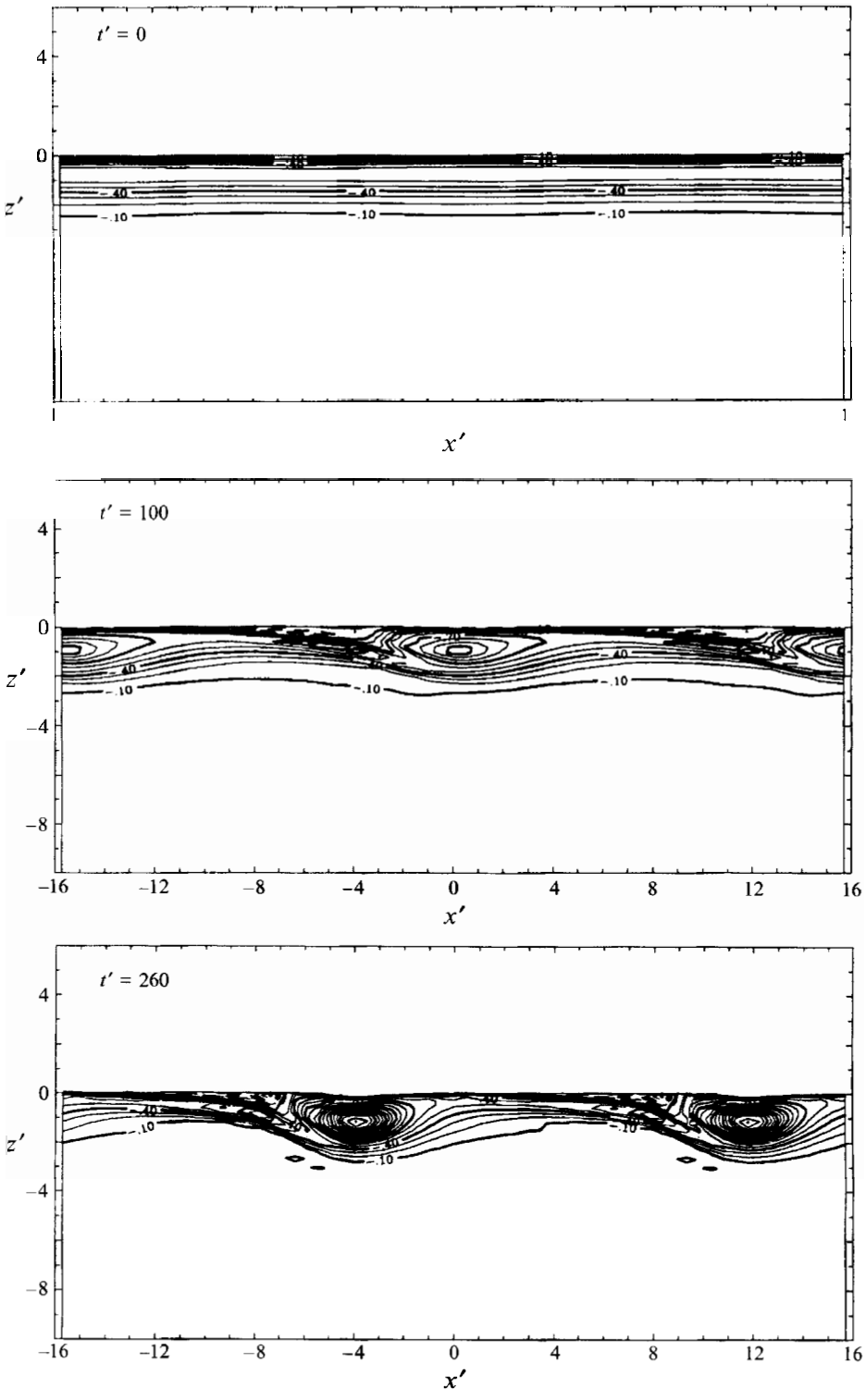

FIGURE 15. Branch I, $F = 0.5$: vorticity contour plots of the total flow at different time instants. Strong vortices are formed below the troughs of the wave, and they rotate counterclockwise. The length in the x-direction is twice the length of the computational domain.

Based on these observations we infer that this free-surface depression will become larger and steeper, resulting in a breaking wave. This observation is in agreement with the numerical results of Tryggvason (1988), who also finds a steep depression on the free surface, and eventually wave breaking, when strong vortices are formed close to the free surface. Interestingly, just before crashing, the wave height remains very small, approximately 1/100 of the wavelength. It is clear, therefore, that the breaking can only be attributed to the presence of velocity shear near the free surface. This can best be seen by looking at the perturbation flow, defined as the total flow minus the mean flow. The vorticity contour plot and the velocity vector plot of the perturbation flow before breaking are shown in figures 12 and 13, respectively. As these plots show, two strong vortices per wavelength are formed in the perturbation flow. The two vortices have opposite signs, and, as a result, the induced horizontal velocities of the perturbation flow at the trough and the crest of the free-surface elevation acquire large magnitudes and opposite signs (figure 14). In other words, a very sharp horizontal velocity shear develops along the free surface, which is responsible for the breaking of the wave. The vertical velocity component remains small throughout the process.

Vorticity contour plots of the total flow, at different time instants, are shown in figure 15. When the initial flow is added to the perturbation flow, it reinforces the vortices that have the same sign as the initial vorticity, and cancels the vortices that have the opposite sign than the initial vorticity. As a result only one vortex per wavelength is present in the total vorticity plot. These vortices have an elongated oval shape, extending for about half the wavelength in the x-direction.

We next consider the evolution of the most unstable Branch I instability wave at a higher Froude number, $F = 1.5$. The linear stability analysis results are: $k = 0.3$, $\omega_r = 0.0813$ ($T = 77.3$), $\omega_i = 0.026$. For the numerical solution, the parameters are: $L = 32$, $N = 64$, $\Delta t = 0.0004$, $D = 12$, $C = 2\pi/k = 15.7$ and $d = 16$. The free-surface elevation $\eta(x', t')$ at different time instants is shown in figure 16. Again, during the early stages of the evolution the free-surface elevation has a sinusoidal shape, and grows according to the linear theory prediction up to time $t' \approx 100$. Then, similarly to the previous case, as nonlinear terms become significant the slope of the free-surface wave becomes steep. The program eventually crashes at time $t' \approx 190$. At the time of breaking, the wave height, although larger than the one reached at $F = 0.5$, is again very small, approximately $\frac{1}{80}$ of the wavelength, The breaking is again caused by the development of a sharp horizontal velocity shear along the free surface (figure 17).

5.3. *Nonlinear evolution of Branch II instability*

In this section we consider the nonlinear evolution of the Branch II instability waves of the parallel flow (45). We, first, consider the evolution of two Branch II instability waves for Froude number $F = 1.5$. The first, with wavenumber $k = 2$, has a growth rate 20% smaller than the maximum, while the second, with wavenumber $k = 1.6$, is the wave with the maximum growth rate.

For the case with $k = 2$, the linear stability analysis results are: $k = 2$, $\omega_r = 1.126$ ($T = 5.58$), $\omega_i = 0.0126$. The parameters used in the numerical simulation are: $L = 16$, $N = 32$, $\Delta t = 0.001$, $D = 8$, $C = 2\pi/k = 3.14$, $d = 16$, and the computation is carried out up to time $t' = 1000$. Again, the computation and the results are presented in a frame of reference that moves with the phase velocity of the linear instability wave. Vorticity contour plots of the flow, at different time instants, are shown in figure 18. The free-surface elevation at different instants in time is shown in figure 19. The variation with time of the amplitude of the free-surface elevation, at the collocation point x_0, is shown in figure 20.

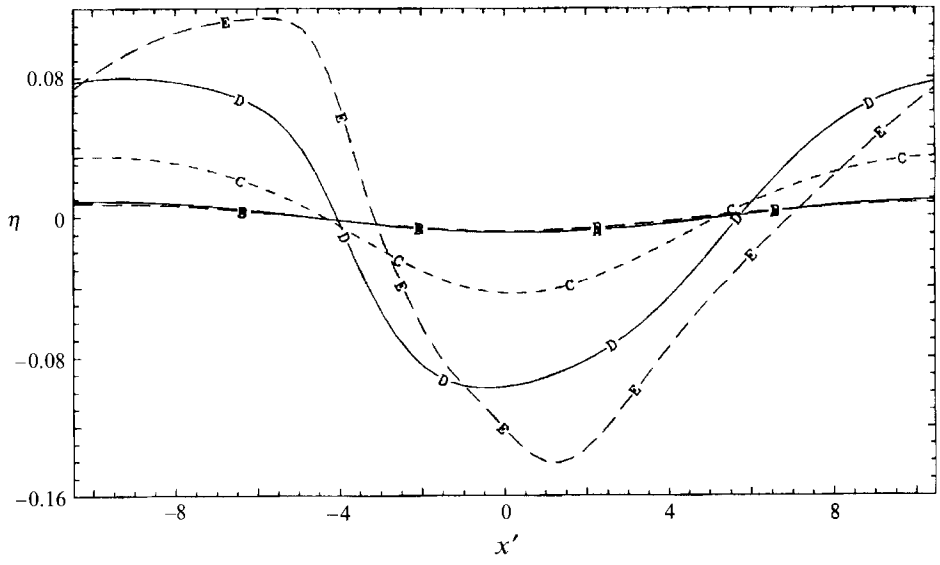

FIGURE 16. Branch I, $F = 1.5$: free-surface elevation $\eta(x', t')$ at different time instants. After the saturation of the instability growth, the wave acquires steep slopes. A, $t' = 0$; B, 50; C, 100; D, 150; E, 190.

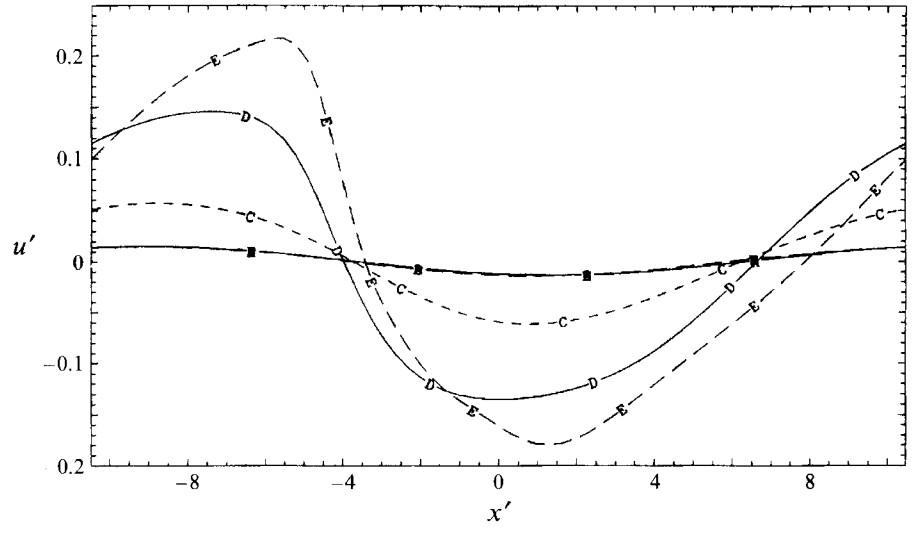

FIGURE 17. Branch I, $F = 1.5$: horizontal velocity $u'(x', z' = \eta, t')$ of the perturbation flow at the free surface and at different time instants. Sharp shear develops before the program crashes. Curves as in figure 16.

The disturbance flow, during the early stages of the flow, grows according to the linear theory prediction, but at time $t' \approx 100$ the instability growth is saturated and the flow approaches asymptotically an equilibrium state, in which the magnitude (of the maximum velocity) of the perturbation flow is about $\frac{1}{10}$ of the initial flow U_∞. Examination of the perturbation flows shows that, as in Branch I waves, two vortices of opposite sign are formed at each wavelength (figure 21). Unlike the low-Froude-

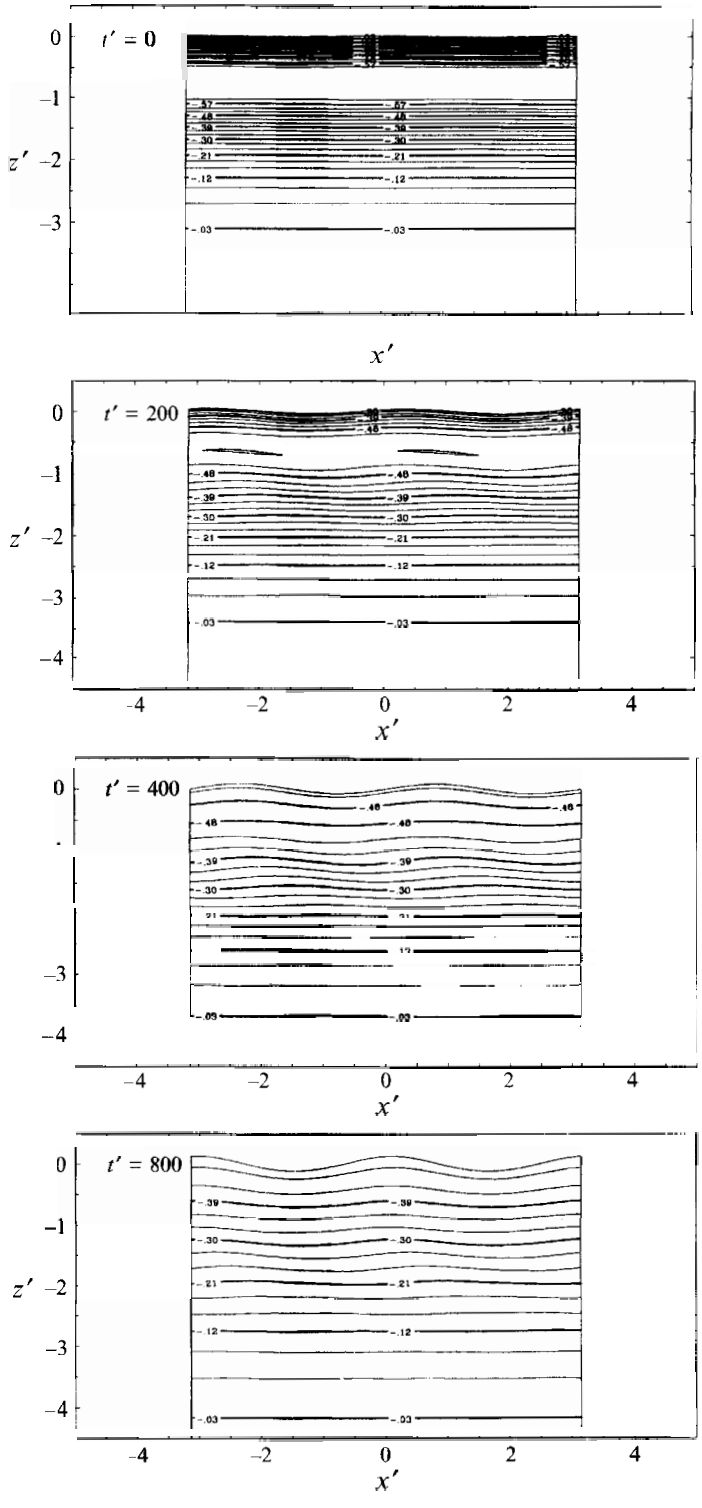

FIGURE 18. Branch II, $F = 1.5$, $k = 2$: vorticity contour plots at different time instants. The flow reaches an equilibrium state, and the vortices are weak. The length in the x-direction is twice the length of the computational domain.

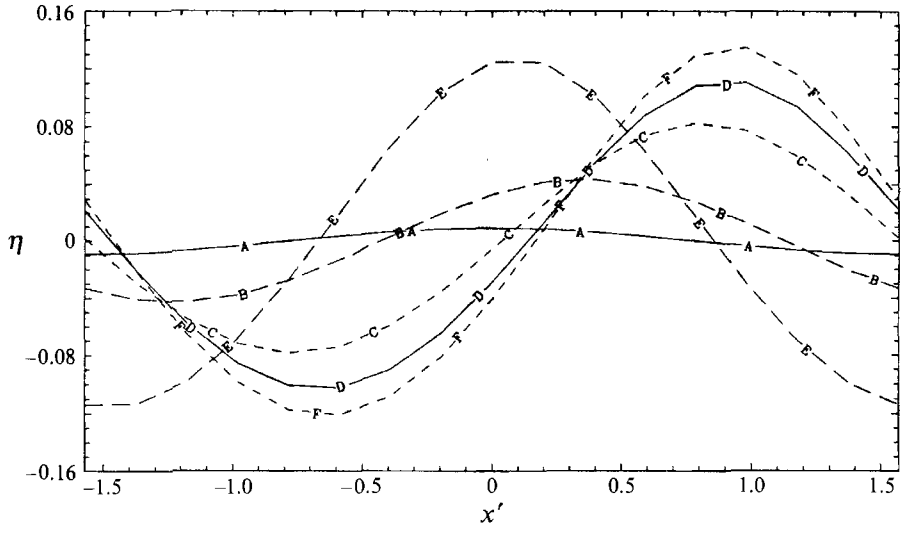

FIGURE 19. Branch II, $F = 1.5$, $k = 2$: free-surface elevation $\eta(x', t')$ at different time instants. The final wave height is substantial ($\frac{1}{12}$ of the wavelength). A, $t' = 0$; B, 200; C, 400; D, 600; E, 800; F, 1000.

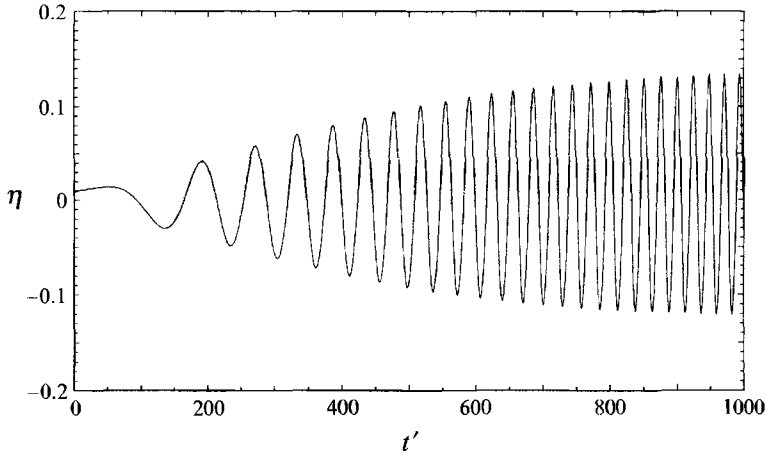

FIGURE 20. Branch II, $F = 1.5$, $k = 2$: free-surface amplitude $\eta(x', t')$ at the collocation point x_0. The frequency of the oscillation changes in the nonlinear regime. It increases by 20% with respect to its linear-regime value.

number Branch I waves, however, the vortices are weak, and their dimensions are small compared to their distance from the free surface. As a result the velocity field at the free surface varies smoothly with x (figure 22), and a propagating surface wave is formed.

The free-surface elevation retains a harmonic shape during the nonlinear stage of the flow, and the final wave height is approximately $\frac{1}{12}$ of the wavelength. The nodes of the free-surface wave can be seen in figure 19 to move downstream along the x-direction. As the plot has been made in a frame of reference that moves with a speed equal to the phase velocity of the linear wave, this implies that the phase velocity of the water wave in the final equilibrium state is larger than the phase velocity during the linear stages

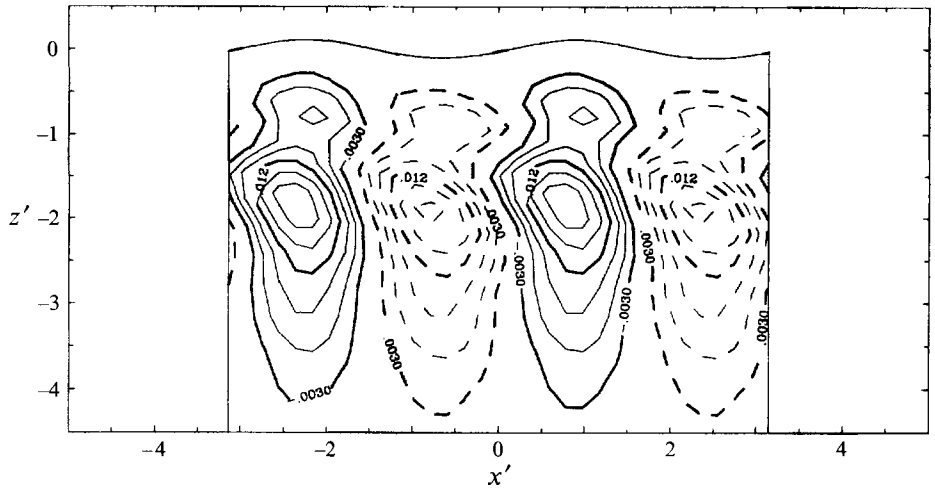

FIGURE 21. Branch II, $F = 1.5$, $k = 2$: vorticity contour plot of the perturbation flow at time $t' = 600$ showing two weak vortices per wavelength with opposite sign of rotation. The length in the x-direction is twice the length of the computational domain.

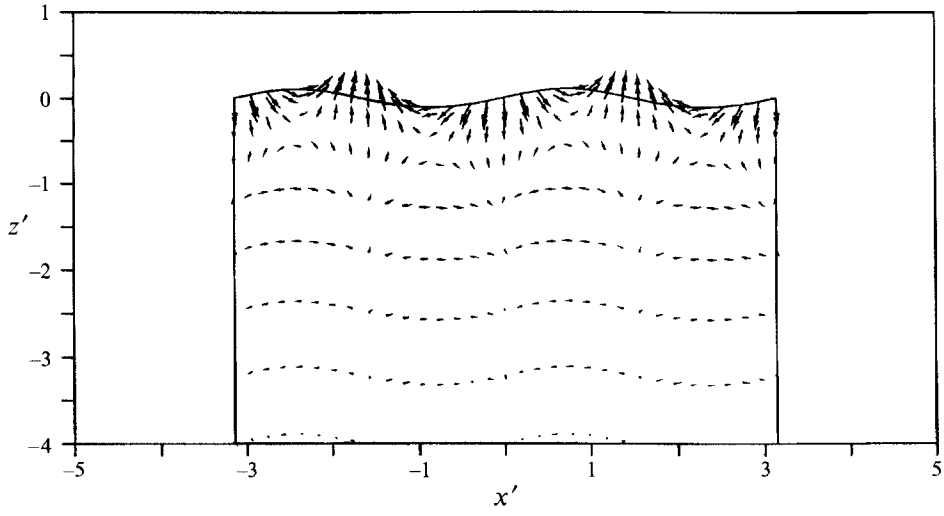

FIGURE 22. Branch II, $F = 1.5$, $k = 2$: velocity vector plot of the perturbation flow at time $t' = 600$. The velocity field variation at the free surface is smooth. The length in the x-direction is twice the length of the computational domain.

of the flow. The same holds for the frequency of the wave. In fact, the frequency of the final state is $\omega_r \approx 1.35$ ($T \approx 4.7$) in the fixed frame of reference, showing an increase of about 20% from its linear theory value. The observed increase of the frequency in the nonlinear regime is consistent with the fact that nonlinearities have a stabilizing effect.

For the wave with the maximum growth rate, we have: $k = 1.6$, $\omega_r = 1.039$ ($T = 6.05$), $\omega_i = 0.0155$. The parameters used in the numerical simulation are: $L = 16$, $N = 32$, $\Delta t = 0.001$, $D = 8$, $C = 2\pi/k = 3.14$, $d = 16$. The computation is carried out up to time $t' = 600$, and the flow approaches asymptotically an equilibrium state. Vorticity contour plots of the flow and the free-surface elevation at different time

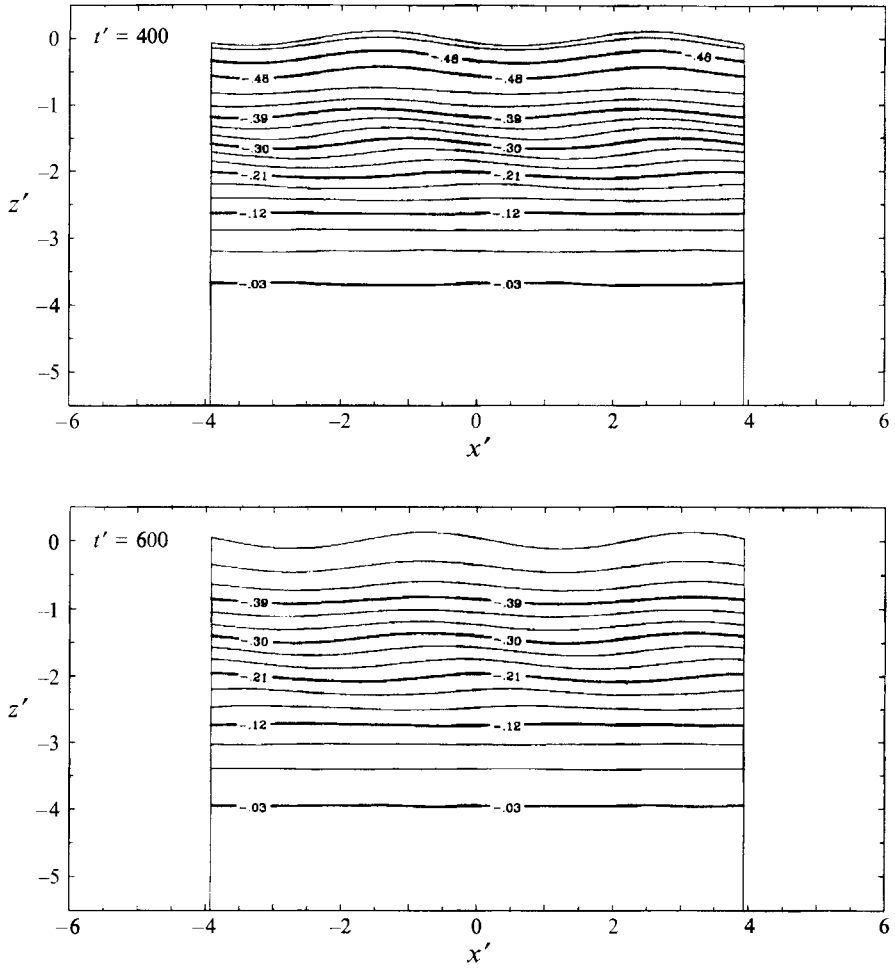

FIGURE 23. Branch II, $F = 1.5$, $k = 1.6$: vorticity contour plots at different time instants. The flow reaches an equilibrium state, and the vortices are weak. The length in the x-direction is twice the length of the computational domain.

instants are shown in figures 23 and 24, respectively. The final results are quite similar to the ones found in the previous simulation for the wave with wavenumber $k = 2$.

We next consider the evolution of the Branch II instability at higher Froude numbers, where the linear-instability growth rates are higher. The linear stability analysis results for the most unstable wave at $F = 2.5$ are: $k = 1.2$, $\omega_r = 0.68$ ($T = 9.2$), $\omega_i = 0.069$. The parameters for the numerical simulation are: $L = 16$, $N = 48$, $\Delta t = 0.00025$, $D = 8$, $C = 2\pi/k = 5.24$ and $d = 16$. The free-surface elevation at different instants in time is shown in figure 25. In this case, the free-surface wave reaches a substantial height, approximately equal to $\frac{1}{12}$ of the wavelength. Unlike the lower-Froude-number cases previously discussed, the computer code crashes at a time $t' \approx 45$, suggesting that the free-surface elevation breaks. At the breaking time, the magnitude of the perturbation flow is roughly $\frac{1}{7}$ of the initial flow.

In figure 25, it is clear that the slope of the free-surface elevation is not very steep, at least for as long as we could carry out the simulation reliably. This suggests that the

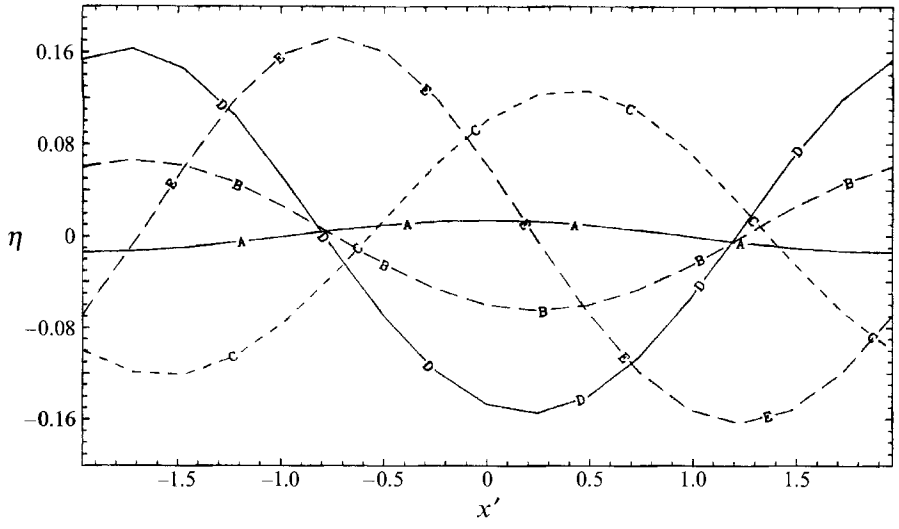

FIGURE 24. Branch II, $F = 1.5$, $k = 1.6$: free-surface elevation $\eta(x', t')$ at different time instants. The final wave height is substantial ($\frac{1}{12}$ of the wavelength). A, $t' = 0$; B, 150; C, 300; D, 450; E, 600.

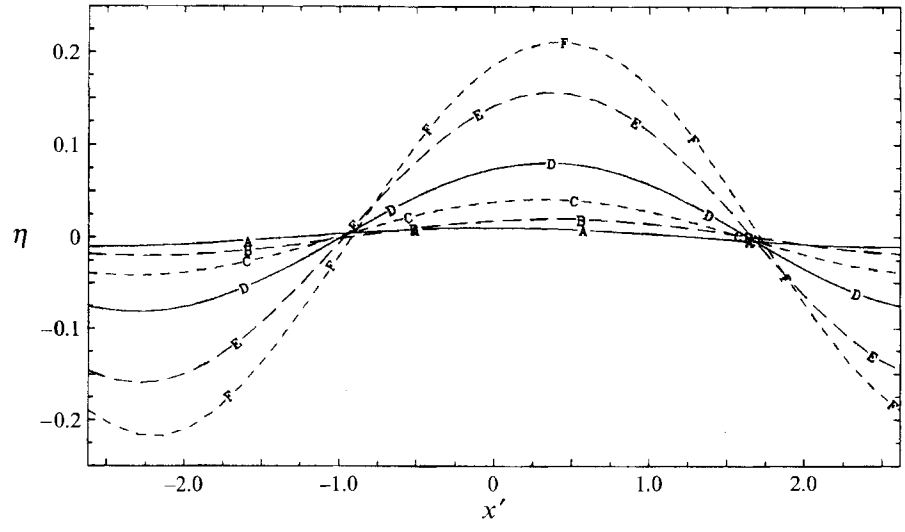

FIGURE 25. Branch II, $F = 2.5$: free-surface elevation $\eta(x', t')$ at different time instants. The wave height reaches a substantial value ($\frac{1}{12}$ of the wavelength) before the wave breaks. A, $t' = 0$; B, 10; C, 20; D, 30; E, 40; F, 45.

mechanics of wave breaking for Branch II waves are different than those of Branch I waves. In fact, breaking of Branch II waves is caused by large variations along the x-axis of the w' velocity component of the flow at the free surface. This can be seen in figure 26, where the partial derivative $\partial w'/\partial x'$ of the vertical velocity component at the free surface is plotted at different time instants: at the initial stages of the instability, the value of $\partial w'/\partial x'$ is small and the corresponding curve has a sinusoidal shape, but at later times the value of the derivative near the trough of the wave increases substantially, showing the presence of strong vertical velocity shear in the horizontal

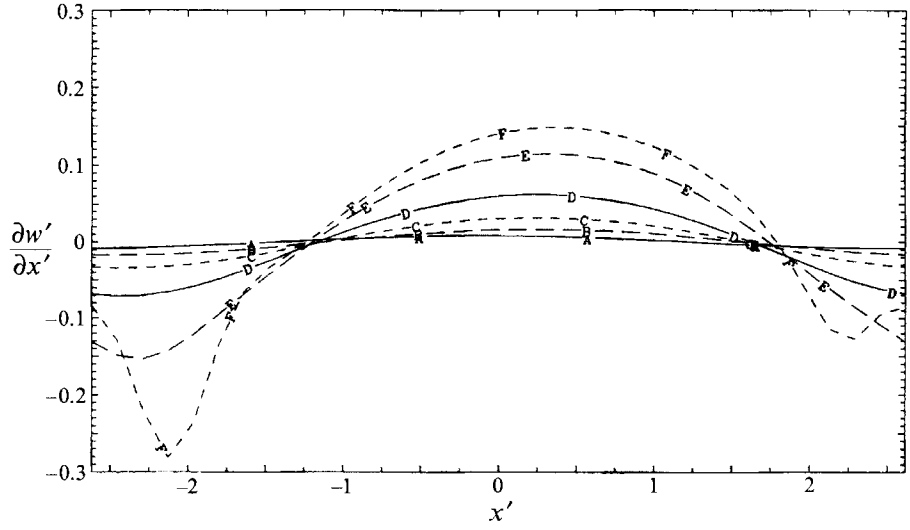

FIGURE 26. Branch II, $F = 2.5$: partial derivative $\partial w'/\partial x'$ of the vertical velocity $w'(x', z' = \eta, t')$ at the free surface and at different time instants. Sharp vertical velocity shear develops at the trough of the free-surface wave. Curves as figure in 25.

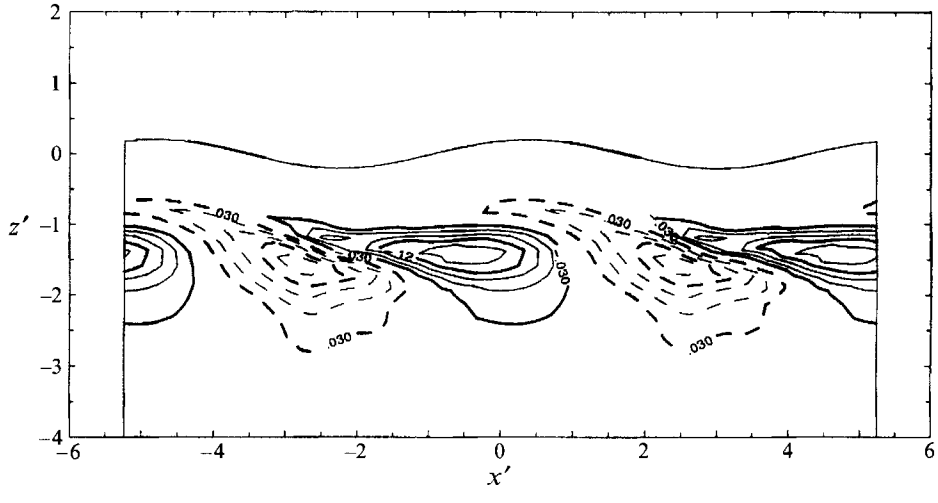

FIGURE 27. Branch II, $F = 2.5$: vorticity contour plot of the perturbation flow at time $t' = 45$. The length in the x-direction is twice the length of the computational domain.

direction. The development of velocity shear at the free surface can be understood by examining the perturbation flow field. In the perturbation flow two vortices with opposite signs are formed per wavelength which generate sharp shear in the vertical velocity component (figures 27 and 28). This sharp vertical velocity shear causes the breaking of the wave, while the horizontal velocities at the free surface remain small.

The same computation is performed for values of Δt ranging from 0.01 to 0.00025 (with L up to 32 and N up to 64), and in all cases the program crashes at about the same time. The plot of the free-surface amplitude $\eta(x', t')$ at the collocation point x_0 (figure 29) shows that the crashing of the program occurs while the instability is still growing

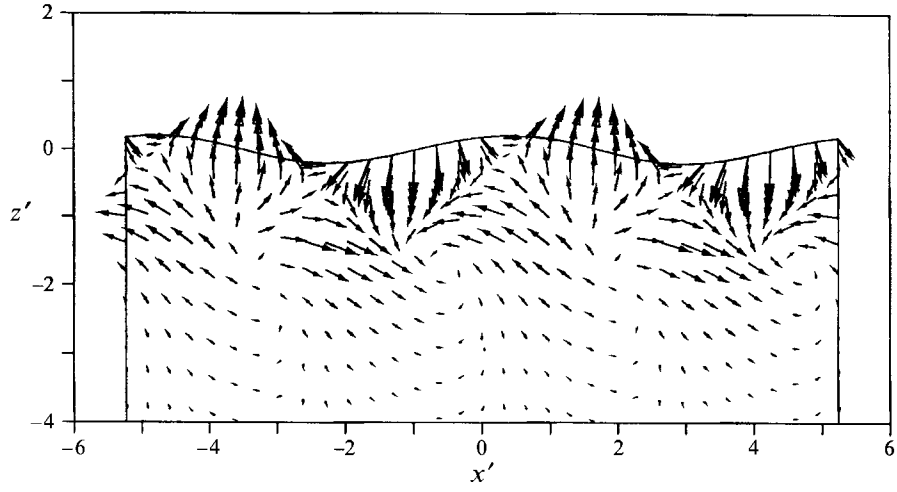

FIGURE 28. Branch II, $F = 2.5$: velocity vector plot of the perturbation flow at time $t' = 45$. The horizontal velocities at the free surface are much smaller than the vertical velocities. The length in the x-direction is twice the length of the computational domain.

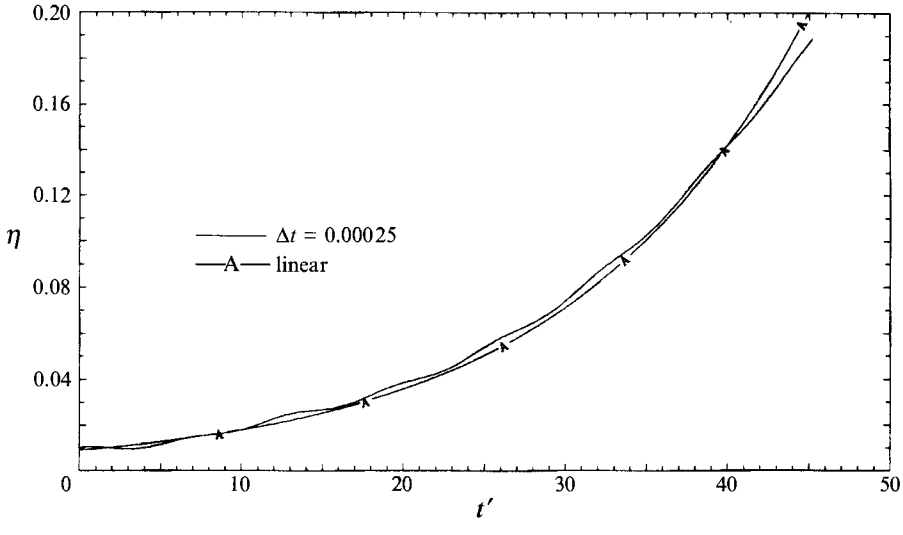

FIGURE 29. Branch II, $F = 2.5$: free-surface amplitude $\eta(x', t')$ at the collocation point x_0. The exponential growth of the linear regime continues till the breaking of the wave.

exponentially in time with the growth rate predicted by linear theory. It seems clear, therefore, that there is a value of Froude number at which the nonlinear evolution of the Branch II waves changes from a propagating wave to a breaking wave; an exact determination of this value is computationally very expensive. Based on the computations that we have conducted, we estimate this value to be somewhat lower than 2.5.

If the Froude number is further increased, the free-surface wave breaks at even earlier times owing to the larger growth rates of the instability. In fact for high-Froude-number flows, the nonlinear evolution of the instability follows very closely that of the

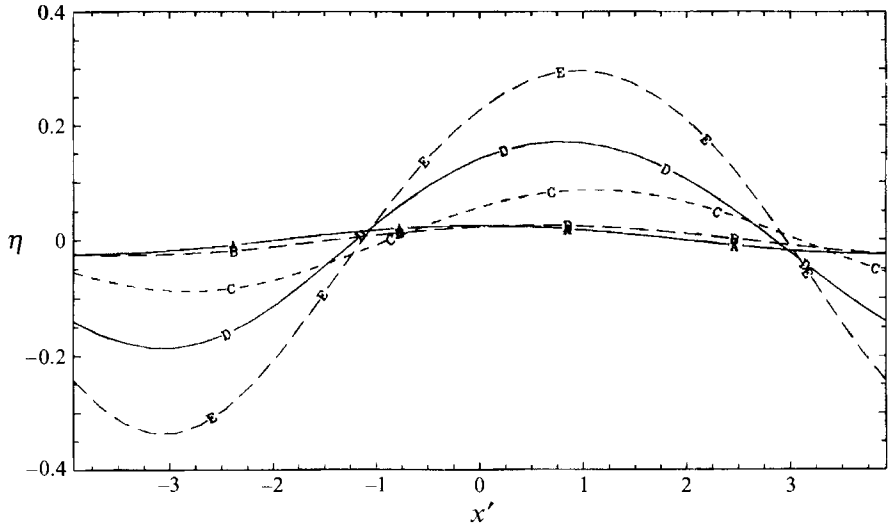

FIGURE 30. Branch II, $F = \infty$: free-surface elevation $\eta(x', t')$ at different time instants. As in the $F = 2.5$ case, the wave height reaches a substantial value ($\frac{1}{12}$ of the wavelength) before the wave breaks. A, $t' = 0$; B, 5; C, 20; D, 15; E, 20.

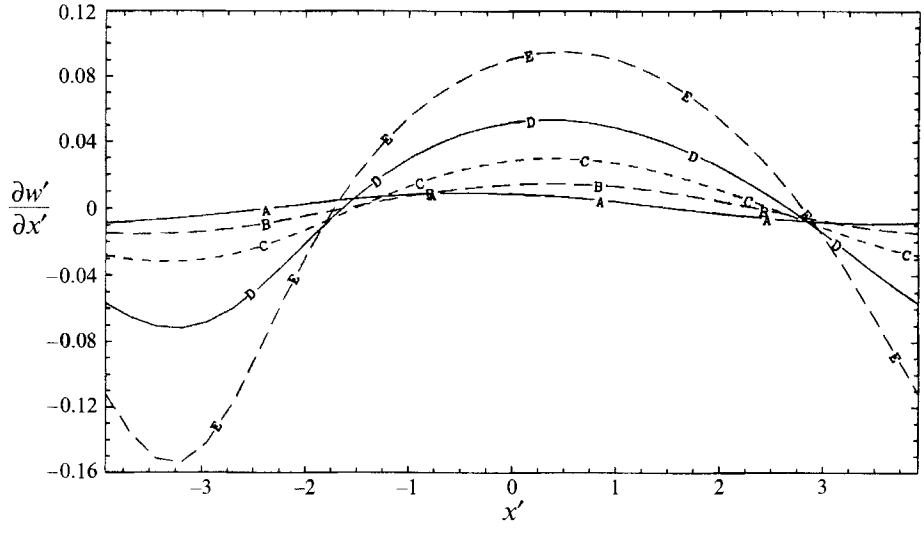

FIGURE 31. Branch II, $F = \infty$: partial derivative $\partial w'/\partial x'$ of the vertical velocity $w'(x', z' = \eta, t')$ at the free surface and at different time instants. Again, sharp vertical velocity shear develops at the free-surface. Curves as in figure 30.

infinite-Froude-number case. For $F = \infty$, the linear stability analysis results (for the most unstable wave) are: $k = 0.8$, $\omega_r = 0.439$ ($T = 14.3$), $\omega_i = 0.141$. For the numerical solution, the parameters are: $L = 16$, $N = 64$, $\Delta t = 0.00025$, $D = 8$, $C = 2\pi/k = 7.85$ and $d = 16$. The free-surface elevation $\eta(x', t')$ at different time instants is shown in figure 30. The amplitude of the partial derivative $\partial w'/\partial x'$ of the vertical component w' of the velocity field at the free surface, at different time instants, is shown in figure 31. The velocity vector plot of the perturbation flow, just before breaking, is shown in figure 32. The free-surface amplitude at the collocation point x_0 as a function

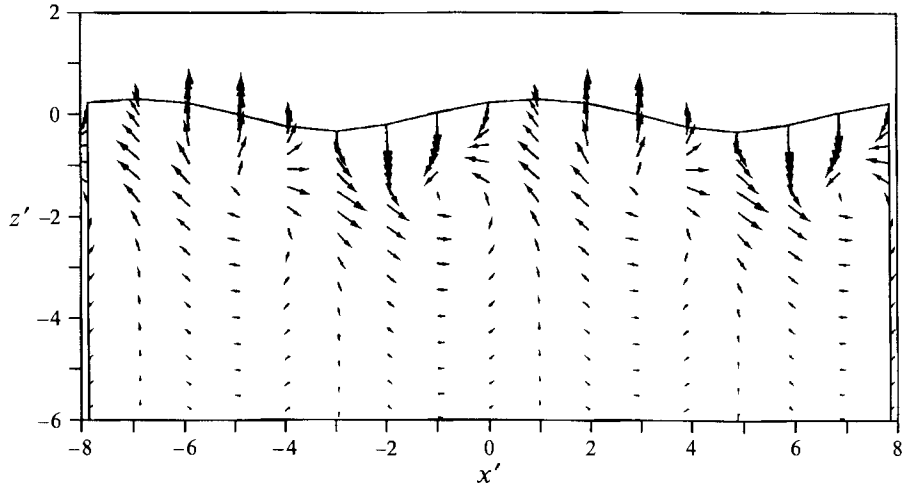

FIGURE 32. Branch II, $F = \infty$: velocity vector plot of the perturbation flow at time $t' = 20$ showing that the strong vertical velocity shear near the troughs and the crests of the free-surface wave persists even in the infinite-Froude-number limit. The length in the x-direction is twice the length of the computational domain.

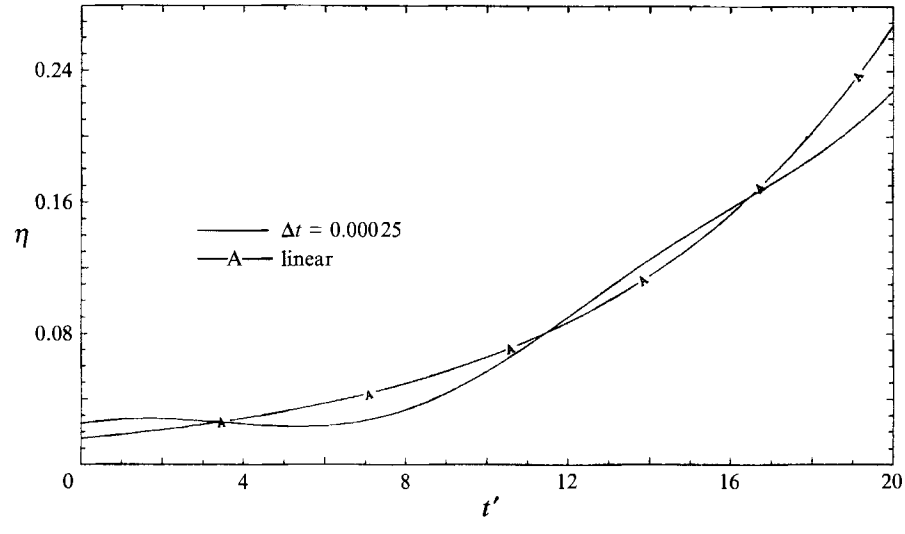

FIGURE 33. Branch II, $F = \infty$: free-surface amplitude $\eta(x', t')$ at the collocation point x_0. The free-surface wave breaks well before the saturation of the linear-regime exponential growth.

of time is shown in figure 33. Vorticity contour plots of the flow, at different time instants, are shown in figure 34. As in the $F = 2.5$ case, the free-surface wave seems to break at a time $t' \approx 20$ during the linear stages of the development of the flow, when the disturbance flow is still growing exponentially in time. At that time the wave height is about $\frac{1}{12}$ of the wavelength, while the perturbation flow is about $\frac{1}{6}$ of the initial flow. The computation was repeated for values of Δt ranging from 0.01 to 0.00025 (with L up to 32 and N up to 96), and, in all cases, the program crashed at about the same time.

We conclude, therefore, that in the infinite-Froude-number limit, the Branch II instability does not reach an equilibrium state. This raises the following interesting question. Based on linear theory, the infinite-Froude-number limit is identical to the

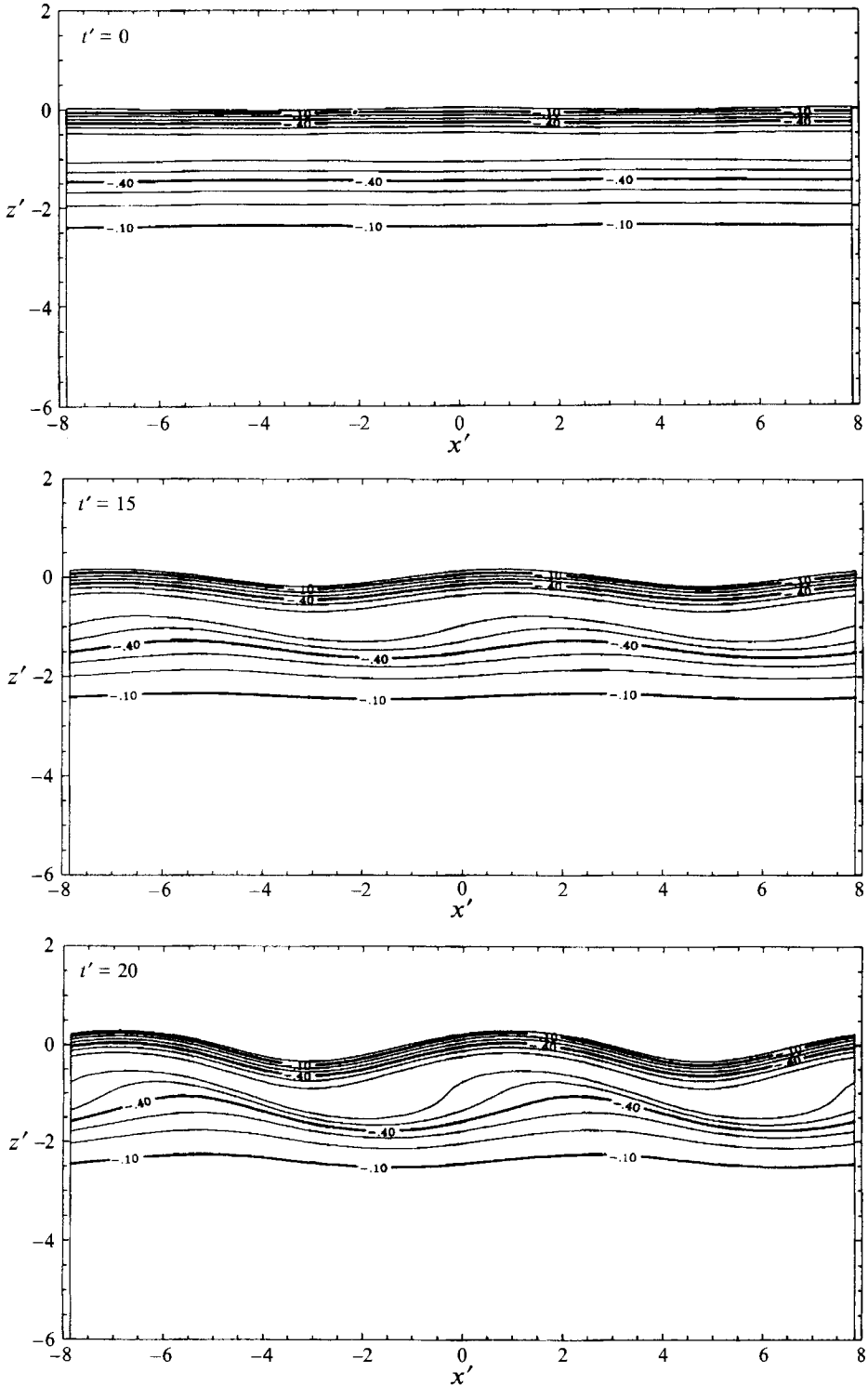

FIGURE 34. Branch II, $F = \infty$: vorticity contour plots at different time instants. The length in the x-direction is twice the length of the computational domain.

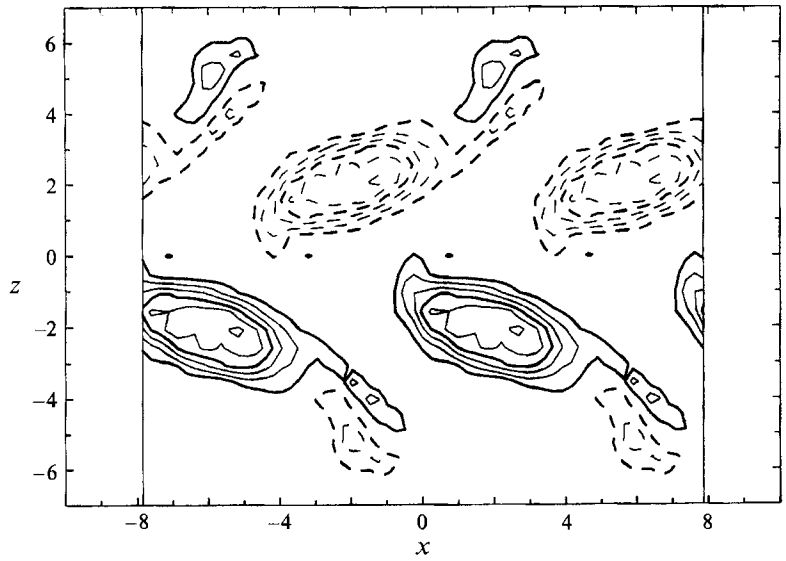

FIGURE 35. Unbounded wake, symmetric stream function mode: vorticity contour plot at time $t = 90$. The flow reaches an equilibrium state where the vortices have the characteristic staggered formation. Solid lines represent negative vorticity, dashed lines represent positive vorticity, the interval between contour levels is 0.12, and the length in the x-direction is twice the length of the computational domain.

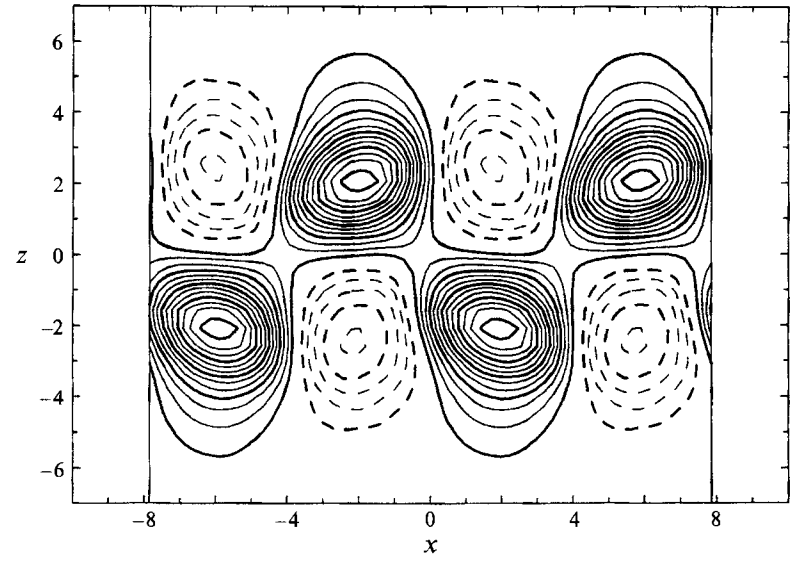

FIGURE 36. Unbounded wake, symmetric stream function mode: Pressure contour plot at time $t = 90$. These is no isopressure line, which has the shape of a possible free-surface elevation. Solid lines represent negative pressure, dashed lines represent positive pressure, the interval between contour levels is 0.01, and the length in the x-direction is twice the length of the computational domain.

symmetric stream function mode of the same velocity profile in unbounded fluid. How similar then is the nonlinear evolution of the flow at the infinite-Froude-number limit to the flow obtained using as an initial condition the symmetric stream function mode? In order to answer this question, we conducted a numerical simulation of the Euler

equations in unbounded fluid using as initial condition the symmetric stream function mode. Interestingly, we found that the flow eventually reaches an equilibrium state. This is demonstrated in figure 35 (vorticity contour plot at time $t = 90$), which shows the formation of a Kármán vortex street. An explanation for the qualitatively different nonlinear behaviour between the infinite-Froude-number limit and the symmetric stream function mode in unbounded fluid can be found by examining the isobars of the equilibrium state of the latter (figure 36). From this plot it is clear that there is no isobar that has the shape of a kinematically admissible free-surface elevation.

6. Conclusions

In this paper we have investigated numerically the two-dimensional nonlinear interaction of an initially parallel shear flow with a free surface. Our investigation was aimed mainly at studying the deformation of the free surface as a result of the growth of the shear flow instability, and the relation of this deformation to the vortical structures formed in the fluid below. In Triantafyllou & Dimas (1989), we found that a shear flow with a free surface possesses two modes of linear instability, corresponding to two different branches of the dispersion relation, named for brevity Branch I and Branch II. The main difference between the two modes from the physical point of view is that Branch I develops a significant horizontal velocity at the free surface, and a very small vertical velocity, whereas Branch II has a substantial vertical velocity at the free surface. This difference is very important in the subsequent nonlinear evolution of the two modes, as the dynamics of Branch I waves seem to be dominated by the variation of the horizontal velocity at the free surface, whereas the dynamics of Branch II waves seem to be dominated by the variation of the vertical velocity at the free surface.

The appearance of very strong shear in either of the two velocity components caused our code to crash; we tentatively identify this behaviour as 'breaking' of the wave. The physical reasons for wave breaking, inferred from the results of the numerical simulation, can be summarized as follows: Branch I and Branch II waves can both create breaking free-surface waves. Although in both cases wave breaking occurs because of the presence of high velocity shear at the ocean surface, the specific mechanics of breaking are quite different. Thus, the breaking of Branch I instability waves is caused by a very sharp variation of the u velocity component with x, while the free-surface elevation remains low (see the sketch in figure 37*a*). In other words, in Branch I breaking, the crest of the wave overtakes the trough of the wave. The breaking of Branch II instability waves, on the other hand, is caused by a very sharp variation of the w velocity component with x, after the wave elevation has reached a substantial value (see the sketch in figure 37*b*). The dynamics of the free-surface elevation are related to the location and strength of the vortices formed in the fluid below, which determine the structure of the induced velocity field at the free surface, as explained in detail in §§ 5.2 and 5.3. We note that the breaking of the Branch I waves is qualitatively similar to that found by Tryggvason (1988) for the free-surface signature of a submerged vortex sheet; there is no equivalent, however, of the Branch II waves for the submerged vortex sheet.

An equilibrium state is therefore reached by the free-surface manifestation only when the variation of both velocity components with x at the free surface is smooth enough to allow the formation of a propagating surface wave. At low Froude numbers, a smoothly varying velocity field is formed only by Branch II instability waves. The shape of these waves seems similar to the symmetric waves of permanent form found by Milinazzo & Saffman (1990). Moreover, the breaking waves that we observed, both

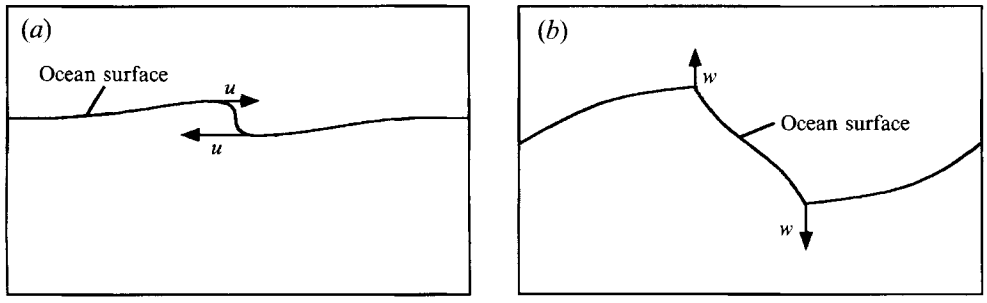

FIGURE 37. (*a*) Sketch of the breaking of Branch I instability waves. Sharp horizontal velocity shear at the free surface breaks the wave, while the wave height remains small. (*b*) Sketch of the breaking of Branch II instability waves. Sharp vertical velocity shear at the free surface breaks the wave, after the wave height has become substantial.

of Branch I and Branch II type, are not symmetric. A quantitative comparison is rather difficult, since the flow in Milinazzo & Saffman (1990) consists of a thin layer of uniform vorticity of low value, whereas the flow in the present study has continuous vorticity with high values.

In summary, the generation of stable propagating surface waves above a shear flow occurs at low Froude numbers for Branch II instability waves. It will be interesting to investigate the effect of three-dimensionality on these waves and on the structure of their vorticity field by allowing the perturbation around the initial state to be three-dimensional.

The financial support of the Office of Naval Research, under contracts N00014-91-J-1287 and N00014-91-J-1373, is greatly appreciated.

REFERENCES

BERNAL, L. P. & KWON, J. T. 1989 Vortex ring dynamics at a free surface. *Phys. Fluids* A **1**, 449–451.

DIMAS, A. A. 1991 Nonlinear interaction of shear flows with the free surface. PhD thesis, Massachusetts Institute of Technology.

DOMMERMUTH, D. G. & YUE, D. K.-P. 1990 A numerical study of three-dimensional viscous interactions of vortices with a free surface. In *Proc. 18th Symp. on Naval Hydrodyn.*, pp. 727–788. National Academy of Sciences, Washington, DC.

DOMMERMUTH, D. G., YUE, D. K.-P., LIN, W. M., RAPP, R. J., CHAN, E. S. & MELVILLE, W. K. 1988 Deep-water plunging breakers: a comparison between potential theory and experiments. *J. Fluid Mech.* **189**, 423–442.

GOTLIEB, D. & ORSZAG, S. A. 1977 *Numerical Analysis of Spectral Methods: Theory and Applications*. SIAM.

HAIDVOGEL, D. B., ROBINSON, A. R. & SCHULMAN, E. E. 1980 The accuracy, efficiency, and stability of three numerical models with application to open ocean problems. *J. Comput. Phys.* **34**, 1–53.

MATTINGLY, G. E. & CRIMINALE, W. O. 1972 The stability of an incompressible two-dimensional wake. *J. Fluid Mech.* **51**, 233–272.

METCALFE, R. W., ORSZAG, S. A., BRACHET, M. E., MENON, S. & RILEY, J. J. 1987 Secondary instability of a temporally growing mixing layer. *J. Fluid Mech.* **184**, 207–243.

MICHALKE, A. 1964 On the inviscid instability of the hyperbolic-tangent velocity profile. *J. Fluid Mech.* **19**, 543–556.

MILINAZZO, F. A. & SAFFMAN, P. G. 1990 Effect of a surface shear layer on gravity and gravity–capillary waves of permanent form. *J. Fluid Mech.* **216**, 93–101.

MYERS, R. B., TAYLOR, T. D. & MURDOCK, J. W. 1981 Pseudo-spectral simulation of a two-dimensional vortex flow in a stratified, incompressible fluid. *J. Comput. Phys.* **43**, 180–188.

OHRING, S. & LUGT, H. J. 1991 Interaction of a viscous vortex pair with a free surface. *J. Fluid Mech.* **227**, 47–70.

ORSZAG, S. A. & KELLS, L. C. 1980 Transition to turbulence in plane Poiseuille and plane Couette flow. *J. Fluid Mech.* **96**, 159–205.

PATERA, A. T. 1984 A spectral element method for fluid dynamics: Laminar flow in a channel expansion. *J. Comput. Phys.* **54**, 468–488.

PATNAIK, P. C., SHERMAN, F. S. & CORCOS, G. M. 1976 A numerical simulation of Kelvin–Helmholtz waves of finite amplitude. *J. Fluid Mech.* **73**, 215–240.

PIERREHUMBERT, R. T. & WIDNALL, S. E. 1982 The two- and three-dimensional instabilities of a spatially periodic shear layer. *J. Fluid Mech.* **114**, 59–82.

SARPKAYA, T. 1986 Trailing-vortex wakes on the free surface. In *Proc. 16th Symp. on Naval Hydrodyn.*, pp. 38–50. National Academy Press.

STUART, J. T. 1967 On finite amplitude oscillations in laminar mixing layers. *J. Fluid Mech.* **29**, 417–440.

TRIANTAFYLLOU, G. S. & DIMAS, A. A. 1989 Interaction of two-dimensional separated flows with a free surface at low Froude numbers. *Phys. Fluids* A **1**, 1813–1821.

TRYGGVASON, G. 1988 Deformation of a free surface as a result of vortical flows. *Phys. Fluids* **31**, 955–957.

WILLMARTH, W. W., TRYGGVASON, G., HIRSA, A. & YU, D. 1989 Vortex pair generation and interaction with a free surface. *Phys. Fluids* A **1**, 170–172.

YU, D. & TRYGGVASON, G. 1990 The free-surface signature of unsteady, two-dimensional vortex flows. *J. Fluid Mech.* **218**, 547–572.